

Erik Jonsson School of Engineering and Computer Science

***Turbulent Flow Over Craters on Mars: Vorticity
Dynamics Reveal Aeolian Excavation Mechanism***

UT Dallas Author(s):

William Anderson

Rights:

©2017 American Physical Society. All Rights Reserved.

Citation:

Anderson, W., and M. Day. 2017. "Turbulent flow over craters on Mars: Vorticity dynamics reveal aeolian excavation mechanism." *Physical Review E* 96(4), doi:10.1103/PhysRevE.96.043110

This document is being made freely available by the Eugene McDermott Library of the University of Texas at Dallas with permission of the copyright owner. All rights are reserved under United States copyright law unless specified otherwise.



Turbulent flow over craters on Mars: Vorticity dynamics reveal aeolian excavation mechanism

William Anderson*

Department of Mechanical Engineering, University of Texas at Dallas, Richardson, Texas 75080, USA

Mackenzie Day

Department of Earth and Space Sciences, University of Washington, 4000 15th Ave NE, Seattle, Washington 98195, USA

(Received 3 July 2017; published 27 October 2017)

Impact craters are scattered across Mars. These craters exhibit geometric self-similarity over a spectrum of diameters, ranging from tens to thousands of kilometers. The late Noachian–early Hesperian boundary marks a dramatic shift in the role of mid-latitude craters, from depocenter sedimentary basins to aeolian source areas. At present day, many craters contain prominent layered sedimentary mounds with maximum elevations comparable to the rim height. The mounds are remnants of Noachian deposition and are surrounded by a radial moat. Large-eddy simulation has been used to model turbulent flows over synthetic craterlike geometries. Geometric attributes of the craters and the aloft flow have been carefully matched to resemble ambient conditions in the atmospheric boundary layer of Mars. Vorticity dynamics analysis within the crater basin reveals the presence of counterrotating helical vortices, verifying the efficacy of deflationary models put forth recently by Bennett and Bell [K. Bennett and J. Bell, *Icarus* **264**, 331 (2016)] and Day *et al.* [M. Day *et al.*, *Geophys. Res. Lett.* **43**, 2473 (2016)]. We show how these helical counterrotating vortices spiral around the outer rim, gradually deflating the moat and carving the mound; excavation occurs faster on the upwind side, explaining the radial eccentricity of the mounds relative to the surrounding crater basin.

DOI: [10.1103/PhysRevE.96.043110](https://doi.org/10.1103/PhysRevE.96.043110)

I. INTRODUCTION AND BACKGROUND

The planetary evolution of Mars, from a warmer planet with surface water to a desiccated planet dominated by aeolian and cryospheric processes, is recorded in its sedimentary rock record. Foremost in this record are sedimentary strata housed within craters occurring on the Noachian terrain of the southern highlands. The best-documented example is Gale Crater, which houses a 5-km mound (Aeolis Mons) of sedimentary strata that is currently being explored by the NASA rover, Curiosity [Fig. 1(b)]. Basal strata within Gale Crater were interpreted as having been deposited by a series of deltas prograding into a long-standing lacustrine water body [1–3]. The mound within Gale Crater is one of a few scores of sedimentary mounds in craters [Fig. 1(a) shows Henry Crater [4]], which are interpreted to represent wind erosional remnants of Noachian times when craters served as major sediment sinks [2,4–8].

Stages of mound formation are thought to progress from sedimentary strata spanning the crater, to development of an initial moat, to retreating central mound, to remnant isolated hill [5]. An alternate interpretation that mounds grew in place via deceleration of sediment-laden katabatic winds [9] has more recently been modified to envision a combination of wind-driven mound erosion and mound-draping layers [10]. With either the prevailing view of the mounds as erosional remnants or the modified mound-growth model with draping layers, understanding wind abrasion of mound strata and transport of eroded sediment from craters is paramount to understanding sediment transport pathways on Mars.

Recently, Day and Kocurek [11] performed a detailed study of aeolian feature morphologies within Gale Crater to

infer intracrater circulations and katabatic winds. Paleowind indicators within and downwind of Gale Crater, including the crater wind streak, yardangs carved into mound strata, and an intracrater landscape developed with progressive wind abrasion, indicate northerly regional winds as paramount in mound formation at Gale Crater. Aeolian features within and adjacent to Gale Crater show that density-driven slope (katabatic) flows and intracrater circulations sustained by larger-scale circulations in the planetary boundary layer of Mars [12–15] are responsible for aeolian processes within the crater. From this work, the observed mound radial eccentricity at other craters can also be attributed to aeolian excavation of crater fill. Moreover, once excavated, crater basins can function as transient depocenters, temporarily housing sediment in the form of sand dunes [16,17], with transport and abrasion sustained by turbulent intracrater circulations.

In a complementary article, Day *et al.* [8] combined innovative wind tunnel experiments and modeling with large-eddy simulation (LES) to study turbulent winds aloft crater geometries. The group was able to demonstrate that secondary flows, originating as vortices shed from the crater upwind rim but forced to realign into counterrotating helical vortices flanking the mound, are responsible for erosion of the moat. This finding confirmed hypotheses put forward on the role of secondary flows [8,9], although rigorous assessment of the mechanisms sustaining turbulent secondary flows and the implications of low-frequency high-magnitude turbulent fluctuations for excavation time scales were not performed. Yet, on Mars, the role of turbulent fluctuations deserves further consideration since preceding contributions [18–20] have shown that the onset of wind-driven mobilization can result in persistent transport.

We note a very recent article from Chan and Netoff [21], who reported wind-excavated terrestrial analogs for the mound-in-crater geometry reported on Mars. Also,

*wca140030@utdallas.edu

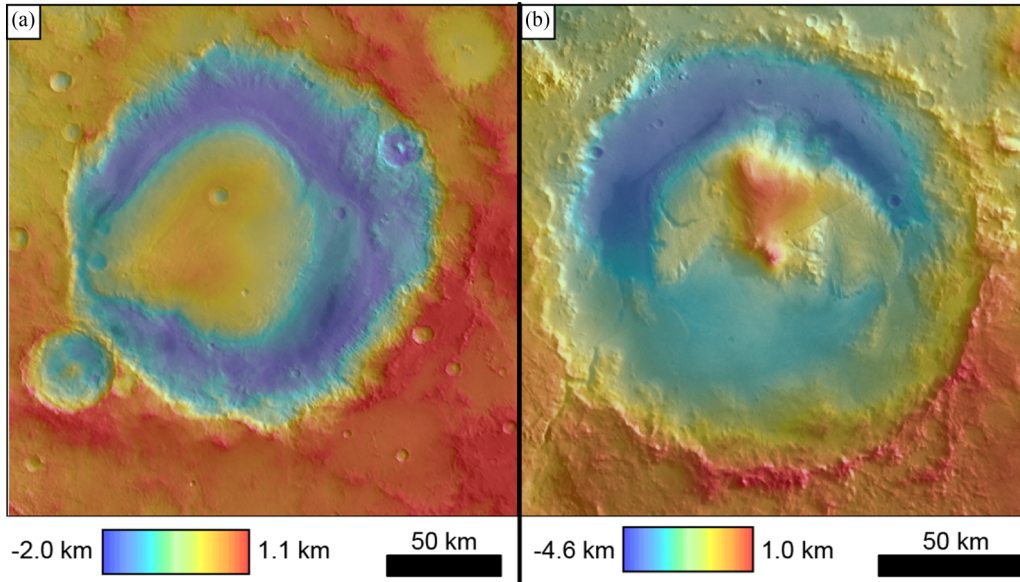


FIG. 1. Digital elevation models of two mid-latitude craters on Mars with interior sedimentary mounds. Colors have been stretched to highlight the crater interior relief of 3.1 and 5.6 km for (a) Henry crater and (b) Gale crater, respectively.

comprehensive meteorological measurements and simulations at Meteor Crater, Arizona, have explored how formation of cold pools is affected by shear aloft the basin [22,23]. However, Meteor Crater is smaller than Gale Crater and simulations of flow over Meteor Crater focused on different aspects of shear-driven mixing aloft the basin.

This study

In this study, we use the LES code from our previous article [8] to fully elucidate the underlying mechanisms responsible for radial excavation of the crater fill. The results are supported by the paleowind reconstruction of Day and Kocurek [11] and are consistent with the concepts put forth by Day *et al.* [8]. That is, vortices shed from the upwind side of the crater rim that split at the centerline undergo spatial realignment via mean flow gradients in the fluid, becoming counterrotating helical vortices that flank the downwind crater rim and sedimentary source areas. In this model, the rotational sense of the counterrotating vortices must entrain high-momentum fluid from aloft, thereby enhancing aerodynamic momentum fluxes and aeolian activity. Results of a series of *a posteriori* flow analysis techniques have been reported. Note that the present simulations are all for neutral stratification and we do not at all consider the influence of radial katabatic winds, although we entirely recognize the importance of katabatic winds as a landscape-altering agent in Mars crater basin morphodynamics [9,10].

The LES code and details of the synthetic crater geometries considered are presented in Sec. II. With this, we show results in Sec. III. Instantaneous and Reynolds- (time-) averaged visualization of differential helicity, a quantity that requires the local coexistence of velocity and vorticity to be nonzero, shows how vortices advect above the crater sedimentary source area. Time-series processing of the streamwise velocity fluctuations at various spatial locations are used to generate probability density functions (PDFs), all of which exhibit a

broad distribution of values, pointing to the prevalence of low-frequency high-magnitude turbulent fluctuations (these being of paramount importance to aeolian activity, especially in the thin atmosphere of Mars [12]). With this, we conditionally sampled the flow during simulations based on exceedance of thresholds defined with the PDFs; the conditionally sampled flow fields all exhibit the counterrotating helical cells hypothesized to exist by Day *et al.* [8].

The Reynolds-averaged transport equation for mean streamwise vorticity is considered, to identify mechanisms responsible for sustenance of the helical vortices. We find that external to the crater, streamwise vorticity gains occur at the expense of vorticity in the spanwise and vertical, both tilted into the streamwise by gradients in the flow. However, within the crater, it is turbulence that contributes most to gains of streamwise vorticity. Wavelet decomposition of time-series velocity is used to demonstrate how the peak spectral density can be attributed to structures with lengths readily attributed to the crater geometry. The article concludes with a rudimentary assessment of the likely excavation time scales that could be realized by aeolian morphodynamics alone. Using a reduced-order treatment, we confirm that the time lapse since the Noachian-Hesperian boundary would be sufficiently long for turbulent winds in the atmosphere of Mars to empty very large mid-latitude craters. A summary is provided in Sec. IV.

II. LARGE-EDDY SIMULATION CODE AND CASES

We consider flow over the Fig. 2 topographies, with attributes summarized in Table I. During LES, the spatially filtered three-dimensional incompressible momentum transport equation is solved at high Reynolds number [24–27] for a neutrally stratified (i.e., no buoyancy forces) turbulent atmospheric boundary layer, absent Coriolis accelerations

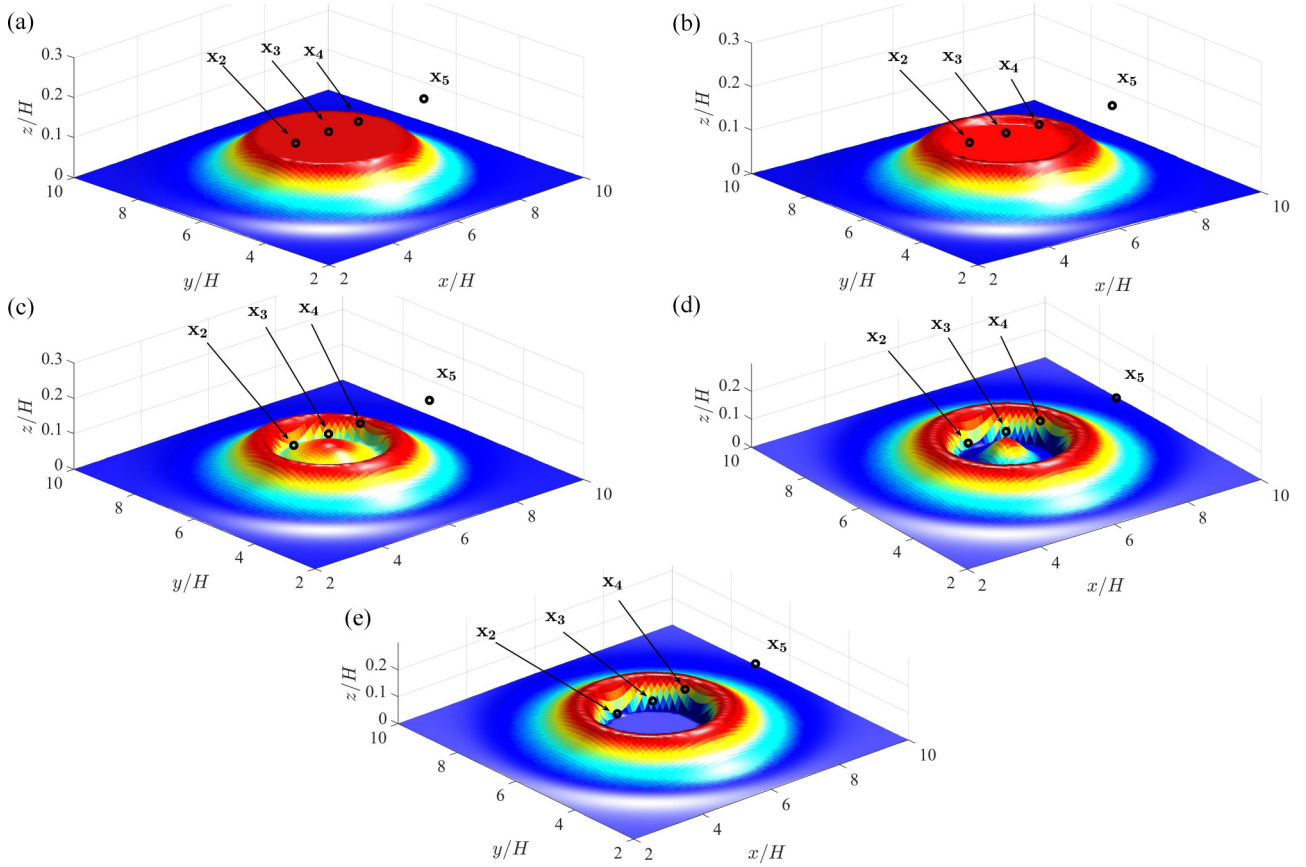


FIG. 2. Perspective images of synthetic craters considered in this study (see also Table I): (a) case 1, (b) case 2, (c) case 3, (d) case 4, and (e) case 5.

(i.e., high Rossby number):

$$\frac{\partial \tilde{\mathbf{u}}}{\partial t} + \frac{1}{2} \nabla (\tilde{\mathbf{u}} \cdot \tilde{\mathbf{u}}) - \tilde{\mathbf{u}} \times \tilde{\boldsymbol{\omega}} = -\frac{1}{\rho} \nabla \tilde{p} - \nabla \cdot \boldsymbol{\tau} + \mathbf{\Pi} + \frac{1}{\rho} \mathbf{f}, \quad (1)$$

where $\tilde{\mathbf{u}}$ is the velocity, a tilde denotes a grid-filtered (LES) quantity, $\tilde{\boldsymbol{\omega}} = \nabla \times \tilde{\mathbf{u}}$ is the vorticity, \tilde{p} is the modified pressure, $\boldsymbol{\tau} = \tilde{\mathbf{u}} \otimes \tilde{\mathbf{u}} - \tilde{\mathbf{u}} \otimes \tilde{\mathbf{u}}$ is the subgrid-scale (SGS) stress tensor, and $\mathbf{\Pi} = \{u_\tau^2/H, 0, 0\}$ is an imposed mean pressure gradient in the streamwise direction, where u_τ is the shear velocity and

TABLE I. Summary of topographic cases considered for the present study, where D is the crater diameter, h is the rim height from the surrounding plane, H is the depth of the atmospheric boundary layer on Mars [14,15], χ is the volumetric ratio of progressive stages of excavation relative to the initially filled state, L is the computational domain length, and N is the resolution of the computational mesh (herein, the mesh has an equivalent number of grid points in the x , y , and z directions).

Case	D/H	h/H	$\chi = V_i/V_1$	L/H	N
1	3.0	0.1	1.0	12.0	128
2	3.0	0.1	0.968	12.0	128
3	3.0	0.1	0.800	12.0	128
4	3.0	0.1	0.787	12.0	128
5	3.0	0.1	0.750	12.0	128

H is the depth of the Martian boundary layer (here we have used $H = 10^4$ m [14]). In this article, the first, second, and third components of any vector correspond to the streamwise, spanwise, and wall-normal directions, respectively (i.e., for the spatial vector $\mathbf{x} = x\hat{i} + y\hat{j} + z\hat{k}$, x , y , and z correspond to the streamwise, spanwise, and wall-normal positions relative to the origin). A solenoidal velocity field is maintained by computing the divergence of Eq. (1), applying the incompressibility condition $\nabla \cdot \tilde{\mathbf{u}} = 0$ and solving the resulting pressure Poisson equation for a pressure correction. Note also that the viscous stresses $\nu \nabla^2 \tilde{\mathbf{u}}$ are omitted from Eq. (1), owing to the high-Reynolds-number fully rough conditions typical of ambient conditions within the crater [the macroscale Reynolds number is $\text{Re}_\tau = U_0 H / \nu \sim O(10^9)$]. The deviatoric component of $\boldsymbol{\tau}$ is evaluated using the eddy-viscosity modeling approach,

$$\boldsymbol{\tau} - \frac{1}{3} \delta \text{Tr}(\boldsymbol{\tau}) = -2\nu_t \tilde{\mathbf{S}}, \quad (2)$$

where Tr denotes the trace operator, δ is the Kronecker delta, $\nu_t = (C_s \Delta)^2 |\tilde{\mathbf{S}}|$ is the turbulent viscosity, C_s is the Smagorinsky coefficient [28], and $\Delta = (\Delta_x \Delta_y \Delta_z)^{1/3}$ is the filter size, where Δ_x , Δ_y , and Δ_z are the computational mesh resolution in the streamwise, spanwise, and vertical directions, respectively. In addition, Δ is the filter scale used to low-pass filter velocity \mathbf{u} , wherein the smoothed velocity field $\tilde{\mathbf{u}}$ is solved in Eq. (1), while the affects of unresolved fluctuations $\mathbf{u}' = \mathbf{u} - \tilde{\mathbf{u}}$ are parametrized via the aforementioned

subgrid-scale model [29]. In addition, $\tilde{\mathbf{S}} = \frac{1}{2}(\nabla\tilde{\mathbf{u}} + \nabla\tilde{\mathbf{u}}^{\text{Tr}})$ is the resolved strain-rate tensor and $|\tilde{\mathbf{S}}| = (2\tilde{\mathbf{S}} : \tilde{\mathbf{S}})^{1/2}$ is magnitude of the resolved strain-rate tensor. For this work, C_s is evaluated dynamically during LES with the Lagrangian scale-dependent dynamic SGS model of Bou-Zeid *et al.* [26]. Pseudospectral discretization is used in the horizontal directions, while vertical gradients are evaluated with centered second-order finite differencing. Periodic boundary conditions are imposed on the vertical planes of the domain, owing to spectral discretization in the horizontal directions. At the domain top, the zero-stress Neumann boundary condition is imposed on streamwise and spanwise velocity $\partial\tilde{u}/\partial z|_{z/H=1} = \partial\tilde{v}/\partial z|_{z/H=1} = 0$. The zero-vertical-velocity condition is imposed on the domain top and bottom $\tilde{w}(x, y, z/H = 0) = \tilde{w}(z, y, z/H = 1) = 0$. Zero-stress Neumann boundary conditions are imposed on the pressure Poisson equation solution at the domain top and bottom $\partial\tilde{p}/\partial z|_{z/H=0} = \partial\tilde{p}/\partial z|_{z/H=1} = 0$. The Adams-Bashforth time-advancement scheme is used for temporal integration of Eq. (1). The nonlinear advection term is dealiased in Fourier space with the 3/2 rule [30]; this is necessary since aliasing errors may contaminate the smallest resolved scales of the flow, compromising predictions of the SGS models. The three-dimensional computational mesh for all simulations is discretized with $N_x = N_y = N_z = N = 128$. Table I summarizes the simulation attributes, where L/H is the domain horizontal length (streamwise and spanwise extent equal for all cases). The computational domain is staggered in the vertical direction; the first computational level for \tilde{u} and \tilde{v} is located at elevation $\frac{1}{2}\Delta_z$.

Here we consider synthetic craters wherein the ratio of rim height h to boundary layer depth H is $h/H = 0.1$. Figure 2 shows the crater cases in perspective. The cases were constructed with superposition of two-dimensional Gaussian functions and are meant to capture canonical geometric representations of craters at progressing deflationary states. Cases 1 and 2 represent the early stages of erosion where the sedimentary fill occupies most of the interior volume of the crater. Examples of these stages include, but are not limited to, Vernal Crater and Asimov Crater. Cases 3 and 4 represent the most visually striking class of craters on this erosional spectrum intermediate between being dominated by the sedimentary fill and the removal of that fill. Craters at this intermediate stage include Croomlin Crater, Firsoff Crater, and Capen Crater. Case 5 represents a typical or empty Martian crater that has been subject to long exposure at the surface but whose resistant rim is less susceptible to erosion than any putative sedimentary material in the crater itself. Examples of such craters include Pollack Crater and Wien Crater. While the craters listed above provide Martian examples approximating the modeled stages, these represent only a few of the many craters on Mars at many scales that exhibit these morphologies. Many more exist, the largest of which have been tabulated by other authors [4]. Table I shows the ratio $\chi = \mathcal{V}_i/\mathcal{V}_1$, where the subscript denotes case number and \mathcal{V} is volume. This ratio provides guidance on the volume of fill removed between cases. With a prescribed boundary layer depth $H = 10^4$ m, Table I shows that the diameters are 30 km, at the lower end of impact crater diameters [4,8]. The diameter to height ratio $D/h = 30$ is of a similar order to real craters on Mars (for example, the diameter and height of Gale

Crater, Pollack Crater, and Capen Crater are 150 and 5 km, 85 and 2.1 km, and 65 and 1.6 km, respectively). Note finally that cases 1–5 are everywhere positive, that is, the internal elevation is not less than the elevation of the surrounding plains. This is a departure from the realities of actual craters [4], where the internal plain is deeper than the surrounding elevation. However, for the purpose of this research, wherein we wish to characterize the deflationary trajectory towards the presently observed states, this constraint does not undermine the relevance to realistic cases. It is reasonable to neglect Coriolis accelerations in Eq. (1) by considering the Rossby number $\text{Ro} = (U/L)\Omega^{-1}$ and substitution of representative scales for the crater circulations $U \sim O(10^1) \text{ m s}^{-1}$, $L \sim 10^3$ m, and $\Omega \sim 10^{-5} \text{ s}^{-1}$, which shows that $\text{Ro} \sim O(10^3)$.

The immersed-boundary method (IBM) used here is based on a wall model that depletes momentum based on the unit-normal area on which the flow impinges [25,31] and the associated drag is added as a body force in the momentum transport equation (1). At spatial locations where the height is less than the first computational grid point for streamwise and spanwise velocity, i.e., $h < \Delta_z/2$, the equilibrium logarithmic law [32,33] is used exclusively to impose aerodynamic drag:

$$\frac{\tau_{i3}^w(x, y, t)}{\rho} = u_\tau^2(x, y, t) = - \left[\frac{\kappa U(x, y, z, t)}{\ln(z/z_0)} \right]^2 \frac{\tilde{u}_i(x, y, z, t)}{U(x, y, z, t)}, \quad (3)$$

where $i = 1$ and 2 correspond to streamwise and spanwise, respectively, κ is the von Kármán constant ($\kappa = 0.4$), $z_0/H = 5 \times 10^{-5}$ is a (momentum) roughness length, \tilde{u}_i denotes the test-filtered velocity, respectively, and $U(x, y, z, t) = [\tilde{u}^2(x, y, z, t) + \tilde{v}^2(x, y, z, t)]^{1/2}$ is the magnitude of the local test-filtered velocity. The choice of such a low z_0 is justified by (i) the plains surrounding the craters being dry barren landscapes and as such are expected to exhibit a very low aerodynamic roughness length [34] and (ii) in the present IBM, where Eq. (3) is used to impose drag at locations where $h < \Delta_z/2$, prescribing a low z_0 ensures that the obstacles, in this case, craters, absorb the largest fraction of the net momentum fluxes. Here we follow Bou-Zeid *et al.* [26] by using the test-filtered velocities for computing the surface stress (3). This approach is typically used for modeling flows over heterogeneous [35] or complex [25] topographies, since it serves to reduce variance of the streamwise and spanwise velocity components close to the wall, thereby improving prediction of the logarithmic law. When $h(x, y) > \Delta_z/2$, the IBM activates a computational body force \mathbf{f} in Eq. (1), based on the spatial variation of the topography $h(x, y)$. The body force is computed via parametrization of local pressure drag

$$\mathbf{F} = - \int_S p^w \mathbf{n} dS, \quad (4)$$

where n_i is the unit-normal vector to $h(x, y)$ and p^w is the resolved wall pressure acting on $h(x, y)$. At entirely immersed cells, the velocity is set to zero. Spectral discretization of Eq. (1) in conjunction with IBM-based drag models is guaranteed to induce small-scale oscillations in the flow, known as the Gibbs phenomenon [36]. This is a natural outcome of using harmonic functions to resolve very sharp boundaries. However, when they are even discernible, these oscillations

manifest as small perturbations superimposed upon the mean flow and as such do not influence scientific conclusions derived from the simulations. This IBM technique (previously named the gradient-based drag modeling technique [25,31]) is used to model pressure drag forces due to p^w . After division by density ρ and local computational cell volume $\Delta_x \Delta_y \Delta_z$, Eq. (4) reduces to a drag force per unit mass required in Eq. (1):

$$\frac{1}{\rho} \mathbf{f} = -\frac{1}{\rho \Delta^2 \Delta_z} \int_S p^w \mathbf{n} dS \approx -\tilde{\mathbf{u}} R(\tilde{\mathbf{u}} \cdot \nabla h) \frac{1}{\Delta_z}, \quad (5)$$

where $R(x)$ is the ramp function [$R(x) = x$ if $x \geq 0$ and $R(x) = 0$ if $x < 0$] and $\partial h / \partial x_k$ ($k = 1$ and 2) is the gradient of $h(x, y)$ in the x and y directions. This use of the ramp function isolates frontal areas of $h(x, y)$ on which \tilde{u}_i impinges. We assume that the drag coefficient $C_d = 2$ for all cases and therefore the typical $\frac{1}{2} C_d$ factor is omitted in Eq. (5) (this implies complete depletion of incoming momentum). The approach was tested against numerous data sets available in the literature for flow over different kinds of topography, e.g., blocks, sinusoids, and ellipsoidal mounds, and in all cases the performance was satisfactory (agreement of time- and plane-averaged streamwise velocity profiles within 10%). For comparison of time- and plane-averaged flow statistics from this modeling technique against literature data sets for a variety of topographies, the interested reader may consult Ref. [31].

III. RESULTS

In this section, results from LES modeling of flow over the crater geometries discussed in Sec. II are presented. We show a range of different results to demonstrate the overarching hypothesis set forth in this article: Counterrotating helical vortices emanating from the upwind crater rim are of pivotal importance to aeolian excavation of large mid-latitude craters on Mars. We first show instantaneous and Reynolds-averaged flow visualizations at various streamwise locations, all demonstrating the presence of counterrotating vortices aloft the crater. We also show visualization of helicity, a quantity useful in understanding mean-flow advection of vorticity. From here, we show results from *a posteriori* assessment of terms contributing to gains and losses in streamwise vorticity. This is accomplished with the Reynolds-averaged streamwise vorticity transport equation, which shows that turbulent mixing within the crater is primarily responsible for sustenance of the rotating crater circulations. This is directly relevant to understanding aeolian excavation. We show PDFs of time-series recordings of streamwise and vertical velocity fluctuations at select locations of dynamical relevance throughout the crater. The PDFs exhibit a wide range of values, consistent with the presence of a wide range of turbulent scales within the crater; the PDFs are also used to conditionally sample the flow, which reveals the spatial attributes of flow structures and surface stress distributions during low-probability high-magnitude events [37,38]. Finally, the time-series measurements are decomposed across constituent frequencies via wavelet transformation, which illustrates how spectral density is distributed to processes occurring at different frequencies. The Strouhal number, a nondimensional measure of vortex shedding frequency [39],

is used to highlight how energy resides at frequencies that can be directly attributed to salient geometric attributes of the crater. The finding is then used to rescale a rudimentary estimate of excavation time scale, which shows that aeolian abrasion and subsequent emptying is a plausible mechanism for crater emptying since the Noachian-Hesperian boundary.

In the following discussion, averaging over dimension a is denoted by $\langle \dots \rangle_a$ (i.e., Reynolds averaging is denoted by $\langle \dots \rangle_t$). Note also that many of the results are presented with visualization in the streamwise- or spanwise-wall-normal planes. In these cases, we emphasize that the figures are greatly exaggerated in the vertical direction, which helps to reveal flow structure aloft the crater.

A. Instantaneous flow visualization

Figure 3 shows visualization of instantaneous streamwise velocity $\tilde{u}(x, t)$ in the streamwise-wall-normal plane [Figs. 3(a) and 3(c)] and spanwise-wall-normal plane [Figs. 3(b) and 3(d)], for cases 2 [Figs. 3(a) and 3(b)] and 4 [Figs. 3(c) and 3(d)]. Line contours of instantaneous streamwise vorticity $\tilde{\omega}_x = \partial \tilde{w} / \partial y - \partial \tilde{v} / \partial z$ are superimposed on the contours. The line contours show that flow aloft the crater is densely populated with counterrotating vortices. The planes were selected to intersect the crater geometric center,

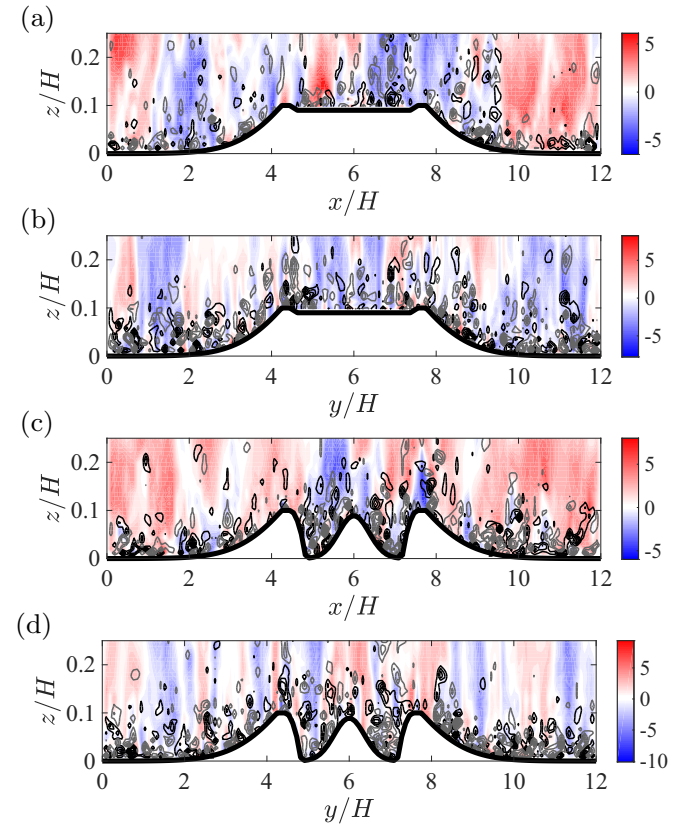


FIG. 3. Visualization of instantaneous flow above (a) and (b) case 2 and (c) and (d) case 4 craters. Color flood contour shows fluctuating streamwise velocity $\tilde{u}' = \tilde{u} - \langle \tilde{u} \rangle_t$, while line contours denote positive (black) and negative (gray) streamwise vorticity $\tilde{\omega}_x$. Panels are retrieved from (a) and (c) $y/H = 6$ and (b) and (d) $x/H = 6$ (see Fig. 2 for reference).

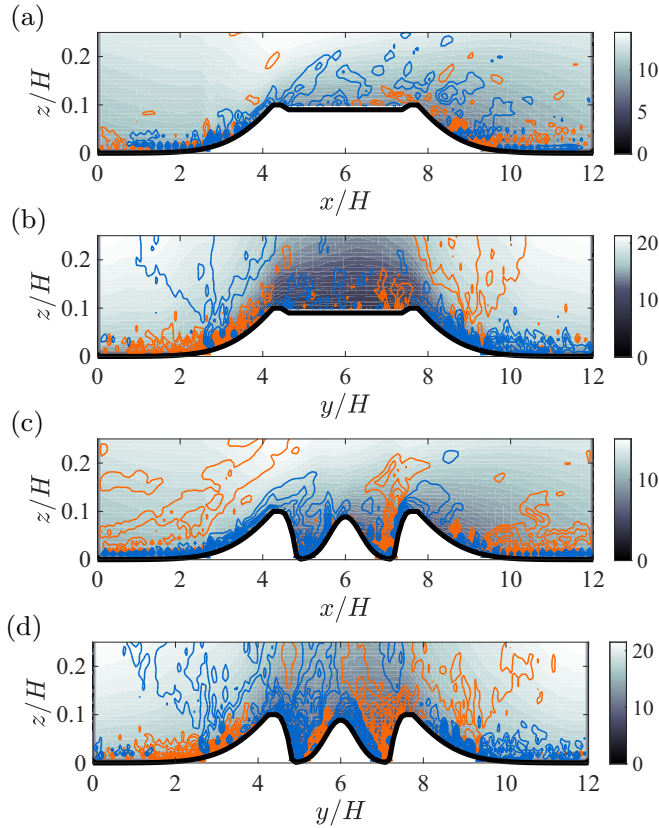


FIG. 4. Visualization of Reynolds-averaged flow above (a) and (b) case 2 and (c) and (d) case 4 craters. Contour shows streamwise velocity $\langle \tilde{u} \rangle_t$, while contours denote positive (orange) and negative (blue) streamwise vorticity $\langle \tilde{\omega}_x \rangle_t$. Panels are retrieved from (a) and (c) $y/H = 6$ and (b) and (d) $x/H = 6$.

and positive and negative line contours of streamwise vorticity have been superimposed. It is difficult to discern order from instantaneous turbulence visualization; the contours certainly show that flow above the crater basin exhibits large fluctuations. Indeed, even after decomposing streamwise vorticity into positive and negative values, no consistent patterns can be readily observed. Figure 3(a) happens to correspond to a time during which flow is being shed from the crater, as observed by the streamwise velocity excess and deficit aloft the upwind and downwind points of the crater rim.

In contrast to the instantaneous visualizations, the Fig. 4 visualizations of Reynolds- (i.e., time-) averaged quantities reveal far more about how the flow responds to the presence of the crater. For cases 2 and 4, Figs. 4(a) and 4(c) shows $\langle \tilde{u} \rangle_t$ and $\langle \tilde{\omega}_x \rangle_t = \partial \langle \tilde{w} \rangle_t / \partial y - \partial \langle \tilde{v} \rangle_t / \partial z$ in a streamwise-wall-normal plane, which reveals how the mean flow is obstructed by the crater. For case 2 [Fig. 4(a)], we see evidence of a shearing layer emanating from the upwind rim (evidenced by region of $\langle \tilde{\omega}_x \rangle_t < 0$ aloft the basin). This is also apparent for case 4 [Fig. 4(c)], although in this case a second shear layer originates at the downwind crater rim. It is in the spanwise-wall-normal plane, however, that features of the flow germane to aeolian excavation become more apparent.

Figure 4(b) reveals the presence of two large counterrotating vortices flanking both sides of the crater (positive in

the region $8 \lesssim y/H \lesssim 10$ and $z/H \gtrsim 0.1$ and negative in the region $1.5 \lesssim y/H \lesssim 4$ and $z/H \gtrsim 0.1$). Application of the right-hand rule shows that $\langle \tilde{\omega}_x \rangle_t > 0$ and $\langle \tilde{\omega}_x \rangle_t < 0$ correspond to counterclockwise and clockwise rotation, respectively. As will be comprehensively shown in subsequent sections, these extracrater circulations are primarily sustained by the tilting of vorticity from the spanwise and vertical dimensions. Closer to the crater, case 2 exhibits two helical vortices at the edges of the crater basin (positive in $7 \lesssim y/H \lesssim 8$ and $0.1 \lesssim z/H \lesssim 0.16$ and negative in $4.5 \lesssim y/H \lesssim 5$ and $0.1 \lesssim z/H \lesssim 0.16$). Again, the right-hand rule indicates that orange and blue correspond to counterclockwise and clockwise rotation, respectively. These helical vortices are argued to be responsible for initiating excavation of the crater sedimentary fill—indeed, surface stress distributions shown in a subsequent section confirm this—and these vortices grow in scale as the moat retreats. For case 4 [Fig. 4(d)], these helical vortices exhibit the same rotational sense, but now engulf almost the entire intracrater space. Now, however, the mound itself is also responsible for shedding of vortices. Using vorticity dynamics analysis, it will be shown that intracrater circulations, the importance of which has now been established from aeolian wind markers within Gale Crater [11], are primarily sustained by turbulence within the crater.

Since the passage of coherent helical vortices is argued to underpin aeolian excavation of the crater fill, it is of interest to assess helicity

$$H_l = \int_{\mathcal{V}} \langle \tilde{\omega} \rangle_t(\mathbf{x}) \cdot \langle \tilde{\mathbf{u}} \rangle_t(\mathbf{x}) d\mathcal{V}, \quad (6)$$

where \mathcal{V} is a control volume over which H_l is to be computed. For our purposes, it is more convenient to consider differential helicity

$$h_l(\mathbf{x}) = \frac{dH_l}{d\mathcal{V}} = \langle \tilde{\omega} \rangle_t(\mathbf{x}) \cdot \langle \tilde{\mathbf{u}} \rangle_t(\mathbf{x}). \quad (7)$$

Figure 5 shows spatial distributions of $h_l(\mathbf{x})$ at streamwise (left) and spanwise (right) positions indicated in the caption. Figures 5(a)–5(h) are for case 1, while Figs. 5(i)–5(p) are for case 4. Since helicity is the inner product of velocity and vorticity, the magnitude of both quantities must simultaneously exceed zero for nonzero local helicity (7). This attribute renders helicity appealing for characterizing the present flows, since it isolates regions where vortex filaments are being advected through the domain (i.e., the helical vortices at the edges of the crater basin that enhance lateral aeolian erosion while simultaneously transporting sediment downwind).

For case 1, in the spanwise-wall-normal plane, we see how the counterrotating helical vortices grow in the downwind direction [Figs. 5(a), 5(c), 5(e), and 5(g) correspond to different downwind locations, as summarized in the figure caption]. At location $x/H = 6$ [Fig. 5(c)], there is a prominent region of $h_l > 0$, which corresponds to $\langle \tilde{\omega}_x \rangle_t > 0$ and $\langle \tilde{u} \rangle_t > 0$ [see Figs. 4(b) and 4(d)]. On the opposite side of the crater, there is a region of equal-and-opposite h_l , due to $\langle \tilde{\omega}_x \rangle_t < 0$. This is the signature of counterrotating circulations, while $h_l \neq 0$ indicates that these vortices are in motion. In the streamwise-wall-normal plane [Figs. 5(b), 5(d), 5(f), and 5(h)], the most prominent feature is the elongated zone of $h_l < 0$ aloft the crater [Fig. 5(f), spanwise location $y/H = 4.875$; see Fig. 2

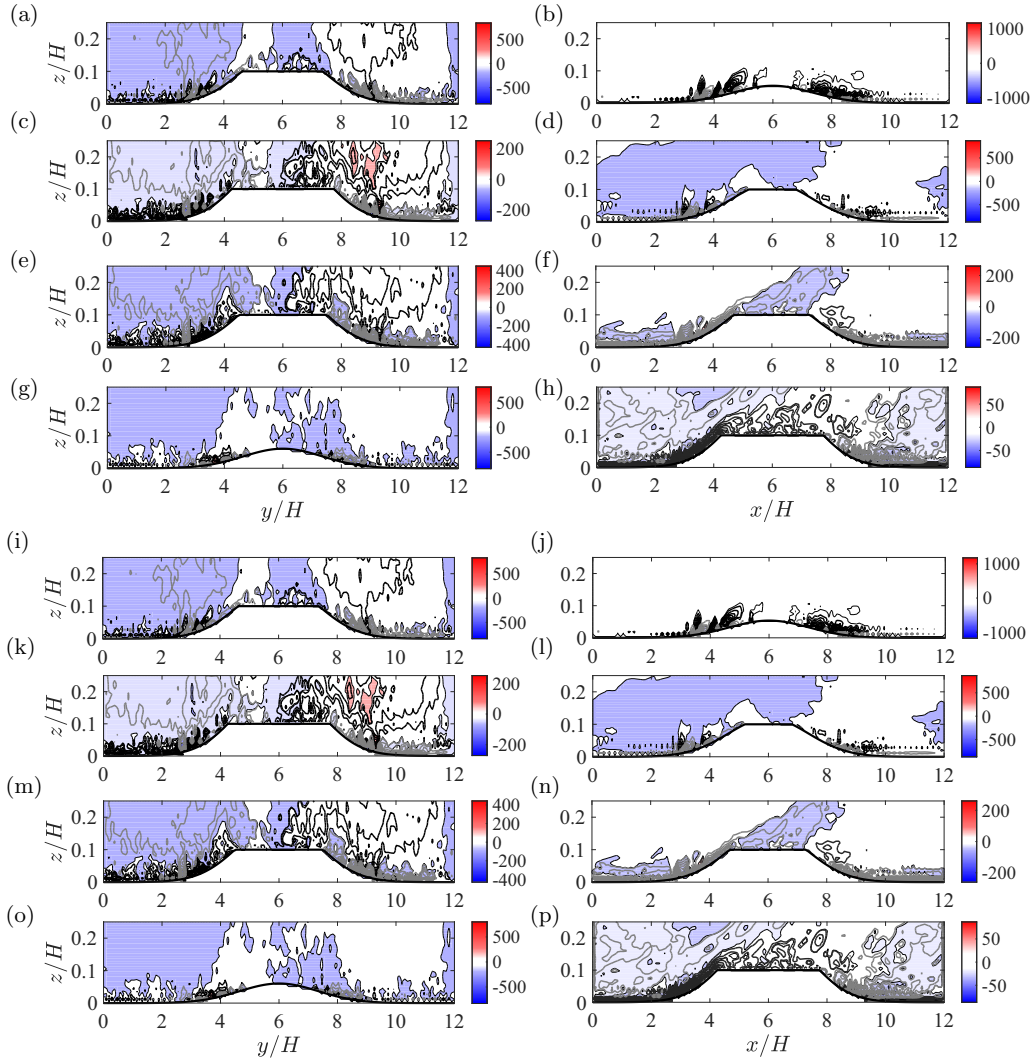


FIG. 5. Visualization of Reynolds-averaged differential helicity (7) for (a)–(h) case 1 and (i)–(p) case 4. Left and right panels are flow visualizations in the spanwise–wall-normal plane and the streamwise–wall-normal plane, respectively, for (a) and (i) $x/H \approx 5$, (c) and (k) $x/H = 6$, (e) and (m) $x/H = 6.94$, (g) and (o) $x/H = 8.25$, (b) and (j) $y/H = 3.75$, (d) and (l) $y/H = 4.5$, (f) and (n) $y/H = 4.875$, and (h) and (p) $y/H = 6$. The color flood contour is h_l , while line contours illustrate Reynolds-averaged streamwise vorticity $\langle \tilde{\omega}_x \rangle_t(\mathbf{x})$, where black and gray denote $\langle \tilde{\omega}_x \rangle_t(\mathbf{x}) > 0$ and $\langle \tilde{\omega}_x \rangle_t(\mathbf{x}) < 0$, respectively.

for reference]. This zone of $h_l < 0$ is sustained by the passage of an air parcel aloft the crater $\langle \tilde{u} \rangle_t > 0$, which also exhibits $\langle \tilde{\omega}_x \rangle_t < 0$. Note that $y/H = 4.875$ corresponds approximately to the lateral edge of the crater basin, where the helical vortices first begin to erode sedimentary fill from the crater. This can be deduced further from Fig. 5(h), from $y/H = 6$, at which $h_l \approx 0$ aloft the crater basin.

For case 4, the flow is more complicated since this case includes a radial moat and mound. Considering first flow patterns in the spanwise–wall-normal plane, Figs. 5(i), 5(k), 5(m), and 5(o) show positive and negative streamwise vorticity at downwind locations $x/H = 5$, 6, 6.94, and 8.28, respectively. The positive and negative vorticity contours demonstrate downwind development of the helical vortices: At $x/H = 5$ [Fig. 5(i)], two distinct counterrotating vortices are apparent, although they are not accompanied by substantial helicity, indicating stationary vortices. However, at $x/H = 6$, these vortices have now moved laterally to the inner wall of the

crater ($y/H \approx 5$ and 7 and there are accompanied by positive and negative helicity, indicating that they are accompanied by coaligned velocity). By $x/H = 6.94$, the vortices are now entirely outside the crater and two new intracrater circulations have formed due to separation from the mound. At $x/H = 6$, these counterrotating vortices flank the mound and grow in diameter by $x/H = 6.94$. By $x/H = 8.25$, only two counterrotating extracrater vortices are present. Interestingly, we see that the vortices at $y/H > 6$ and $y/H < 6$ exhibit clockwise and counterclockwise rotation, respectively.

Figures 5(j), 5(l), 5(n), and 5(p) illustrate differential helicity in the streamwise–wall-normal plane at spanwise locations $y/H = 3.75$ (outside crater), 4.5 (lateral rim), 4.875 (inside moat), and 6 (centerline), respectively, for case 4. This series of figures thus illustrates lateral mean flow patterns associated with the $\langle \tilde{\omega}_x \rangle_t < 0$ parcel reported in Figs. 5(i), 5(k), and 5(m). We see that the most prominent region of $h_l \neq 0$ occurs at $y/H = 4.875$, which, as shown in Fig. 2, is just inside

the crater rim. This region of high magnitude h_l somewhat resembles the pattern for case 1 [Fig. 5(f)], although now the region of $h_l < 0$ originates within the crater basin, highlighting how the radial helical vortices continue to plunge lower into the crater as sedimentary fill is removed. Thus, once the process of aeolian excavation was set in motion, progressive erosion was ensured by virtue of a flow-geometry feedback with the deflating crater basin geometry. The trajectory results first in deflation of the moat and then erosion of the mound [8].

As noted in Sec. II, the simulations are vulnerable to benign numerical contamination due to the Gibbs phenomenon [36]. This can be observed in Figs. 5(b), 5(d), 5(l), 5(n), and 5(p) as unphysical spots superimposed on top of the mean flow. The Gibbs phenomenon is a natural consequence of spectral discretization in simulations with sharp spatial gradients and its presence does not undermine scientific conclusions derived from the simulations.

The results presented in this section help to illustrate the mean flow patterns, but do not identify the mechanisms responsible for sustenance of the helical vortices or their impact on aeolian erosion. In the following section, a vorticity dynamics analysis of the Reynolds-averaged flow is performed, which allows isolation of terms responsible for vortex sustenance throughout the domain spatial extent. The results demonstrate that turbulent fluctuations are overwhelmingly responsible for intracrater circulations. This result necessitates conditional sampling of the flow, in order to visualize the structural nature of the helical vortices present during high-magnitude fluctuations. The results culminate in presentation of a structural model in which processes contributing to streamwise rotation are summarized, while another graphic is presented to summarize the deflationary trajectory of the crater basin.

B. Vorticity dynamics and secondary flow dynamics

Vorticity dynamics is an ideal tool for studying the present flows, in which vortices shed from the rim are of pivotal importance to aeolian excavation of the crater fill. Throughout this analysis, we will show that the classical stretching-and-tilting mechanisms play a relatively small role in sustenance of the helical vortices and it is in fact turbulent secondary flows that dominate intracrater circulations [40–42]. The procedure begins with consideration of the Reynolds-averaged momentum transport equation, which differs distinctly from the grid-filtered (or large-eddy) momentum transport equation (1), shown here as

$$\begin{aligned} & \frac{1}{2} \nabla \cdot (\langle \tilde{\mathbf{u}} \rangle_t \cdot \langle \tilde{\mathbf{u}} \rangle_t) - \langle \tilde{\mathbf{u}} \rangle_t \times \langle \tilde{\boldsymbol{\omega}} \rangle_t \\ & = -\frac{1}{\rho} \nabla \tilde{p} - \nabla \cdot \langle \mathbf{T} \rangle_t + \mathbf{\Pi} + \frac{1}{\rho} \mathbf{f}, \end{aligned} \quad (8)$$

where $\langle \dots \rangle_t$ denotes a Reynolds-averaged quantity and $\langle \mathbf{T} \rangle_t = \langle \mathbf{u}' \otimes \mathbf{u}' \rangle_t$ is the Reynolds stress tensor. The curl of Eq. (8) yields the Reynolds-averaged vorticity transport equation

$$\underbrace{\langle \tilde{\mathbf{u}} \rangle_t \cdot \nabla \langle \tilde{\boldsymbol{\omega}} \rangle_t}_{\text{advection}} = \underbrace{\langle \tilde{\boldsymbol{\omega}} \rangle_t \cdot \nabla \langle \tilde{\mathbf{u}} \rangle_t}_{\text{stretching and tilting}} - \underbrace{\nabla \times \nabla \cdot \langle \mathbf{T}_{ij} \rangle_t}_{\text{turbulent torque}}, \quad (9)$$

where the curls of the pressure correction ∇p , pressure-gradient forcing $\mathbf{\Pi}$, and imposed body force \mathbf{f} vanish by virtue of being parallel to the grad operator ∇ . The role of constituent terms in Eq. (9) have been annotated with underbraces, for discussion.

The stretching-and-tilting term describes how vorticity is reoriented, or tilted, from orthogonal dimensions via ambient spatial gradients in momentum and how vorticity in the transport dimension is amplified or suppressed via a mean-flow gradient in the same dimension (a common analogy for the stretching mechanism is the motion of a pirouetting ballerina, whose rate of rotation is modulated by vertically stretching). The presence of the turbulent torque term is a manifestation of consideration of the Reynolds-averaged transport equation and quantifies how spatial gradients of terms within the Reynolds-stress tensor can sustain turbulent secondary flows [40]. The preceding transport equation can be decomposed into its three Cartesian components for each term in the Reynolds-averaged vorticity vector $\langle \tilde{\boldsymbol{\omega}} \rangle_t = \langle \tilde{\omega}_x \rangle_t \hat{i} + \langle \tilde{\omega}_y \rangle_t \hat{j} + \langle \tilde{\omega}_z \rangle_t \hat{k}$. However, the focus of the present article is principally transport of $\langle \tilde{\omega}_x \rangle_t$ and to that extent we consider only the streamwise component of Eq. (9), expanded here using index notation

$$\underbrace{\langle \tilde{\mathbf{u}} \rangle_t \cdot \nabla \langle \tilde{\omega}_x \rangle_t}_{\text{advection}} = \underbrace{\langle \tilde{\boldsymbol{\omega}} \rangle_t \cdot \nabla \langle \tilde{\mathbf{u}} \rangle_t}_{\text{stretching and tilting}} - \underbrace{\epsilon_{xqi} \partial_q \partial_j \langle \mathbf{T}_{ij} \rangle_t}_{\text{turbulent torque}}. \quad (10)$$

Index expansion of the stretching-and-tilting term $\langle \tilde{\omega}_x \rangle_t \partial_x \langle \tilde{\mathbf{u}} \rangle_t + \langle \tilde{\omega}_y \rangle_t \partial_y \langle \tilde{\mathbf{u}} \rangle_t + \langle \tilde{\omega}_z \rangle_t \partial_z \langle \tilde{\mathbf{u}} \rangle_t$ shows how gains or losses in streamwise vorticity can be sustained by streamwise gradients in $\tilde{\mathbf{u}}$ and via tilting of spanwise and vertical vorticity by spanwise and vertical gradients in $\langle \tilde{\mathbf{u}} \rangle_t$, respectively. Moreover, index expansion of the turbulent torque term $\epsilon_{xqi} \partial_q \partial_j \langle \mathbf{T}_{ij} \rangle_t = (\partial_y^2 - \partial_z^2) \langle \mathbf{T}_{yz} \rangle_t + \partial_{yz} (\langle \mathbf{T}_{zz} \rangle_t - \langle \mathbf{T}_{yy} \rangle_t) + \partial_{xy} \mathbf{T}_{xz} + \partial_{xz} \mathbf{T}_{xy}$ shows that gains or losses in $\langle \tilde{\omega}_x \rangle_t$ are associated with all components of \mathbf{T}_{ij} , with the exception of the streamwise-normal component \mathbf{T}_{xx} .

Figures 6 and 7 show spanwise-wall-normal contours of constituent right-hand-side terms of Eq. (10), as denoted by the figure annotations. The left and right panels correspond to streamwise locations $x/H = 5$ and 6, respectively. It is clear, first, that the stretching term [Figs. 6(a), 6(b), 7(a), and 7(b)] makes a virtually negligible contribution to $\langle \tilde{\omega}_x \rangle_t$ at both streamwise locations. Moreover, the tilting terms for spanwise and vertical vorticities make an approximately equal-and-opposite contribution to $\langle \tilde{\omega}_x \rangle_t$ transport [Figs. 6(c)–6(f) and 7(c)–7(f)], where the balance mainly contributes to extracrater circulations flanking the crater walls [Figs. 6(i), 6(j), 7(i), and 7(j)]. Turbulent torque, on the other hand, is elevated across the crater exterior walls and basin, and the signature of this term is evident in the sum of terms [Figs. 6(k), 6(l), 7(k), and 7(l)]. Note also that turbulent torque is negative and positive for $x/H \lesssim 6$ and $x/H \gtrsim 6$, respectively, which shows that turbulence, not stretching and tilting via the mean flow, sustains the helical vortices that arc around the basin. These counterrotating vortices exhibit downwind advection, as summarized in the preceding section on differential helicity (Fig. 5 and accompanying text), and are of special relevance to aeolian erosion since the presence of events that are infrequent, but high magnitude, can elevate the local aerodynamic stresses far beyond what the mean flow

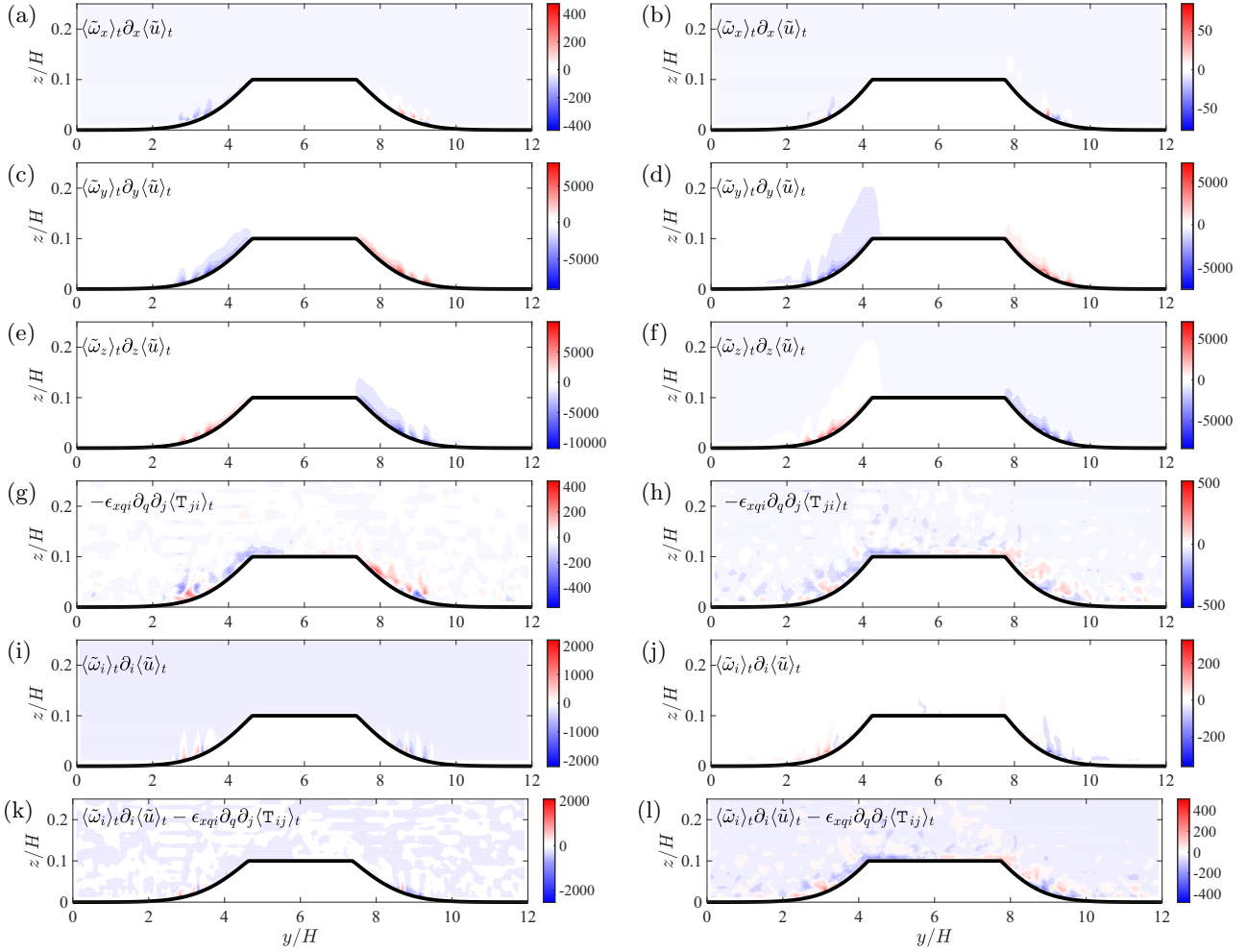


FIG. 6. Visualization of constituent terms from the Reynolds-averaged streamwise vorticity transport equation for flow over case 1 at streamwise positions $x/H \approx 5$ (left panels) and $x/H = 6$ (right panels) (see Fig. 2 for reference), showing (a) and (b) stretching of $\langle \tilde{\omega}_x \rangle_t$ by $\partial_1 \langle \tilde{u}_1 \rangle_t$, (c) and (d) tilting of $\langle \tilde{\omega}_2 \rangle_t$ by $\partial_2 \langle \tilde{u}_1 \rangle_t$, (e) and (f) tilting of $\langle \tilde{\omega}_3 \rangle_t$ by $\partial_3 \langle \tilde{u}_1 \rangle_t$, (g) and (h) production of $\langle \tilde{\omega}_1 \rangle_t$ by turbulent torque, (i) and (j) the sum of $\langle \tilde{\omega}_1 \rangle_t$ gain and loss via mean-flow gradients, and (k) and (l) the sum of terms contributing to the gain and loss of $\langle \tilde{\omega}_1 \rangle_t$.

could develop [38]. A discussion on turbulence and aeolian activity is left for a subsequent section.

To summarize this result, we present the Fig. 8 structural model of flow aloft the crater and mechanisms sustaining the helical vortices; the sketch actually pertains to an emptied crater, although the basic attributes of this figure are helpful to understanding vorticity dynamics aloft the case 1 crater. Here $\partial_y \langle \tilde{u}_1 \rangle_t < 0$ and $\partial_y \langle \tilde{u}_1 \rangle_t > 0$ for $y/H \lesssim 6$ and $y/H \gtrsim 6$, respectively, by virtue of aerodynamic drag on the crater, as has been sketched in Fig. 8 [see also Figs. 4(b) and 4(d)]. Meanwhile, $\langle \tilde{\omega}_y \rangle_t = \partial_z \langle \tilde{u}_1 \rangle_t - \partial_x \langle \tilde{w} \rangle_t \approx \partial_z \langle \tilde{u}_1 \rangle_t$, since the streamwise variation in vertical velocity will be modest relative to the wall-normal gradient in streamwise velocity owing to net drag on the crater. Thus, the sign of $\partial_y \langle \tilde{u}_1 \rangle_t$ sets the resultant sign of streamwise vorticity to be gained by tilting of $\langle \tilde{\omega}_y \rangle_t$, as shown in Figs. 6(c) and 6(d).

Similarly, the vertical gradient of streamwise velocity must be everywhere positive on the upwind side of the external crater face, again by virtue of net drag on the crater [see also Figs. 4(a) and 4(c)]. Here $\langle \tilde{\omega}_z \rangle_t = \partial_x \langle \tilde{v} \rangle_t - \partial_y \langle \tilde{u}_1 \rangle_t \approx -\partial_y \langle \tilde{u}_1 \rangle_t$, again since the streamwise dependence of momentum is

far weaker than the spanwise or wall-normal dependence (recall the preceding discussion). Thus, since $\partial_y \langle \tilde{u}_1 \rangle_t$ and $\langle \tilde{\omega}_z \rangle_t$ have opposing signs, it can be deduced that $\partial_z \langle \tilde{u}_1 \rangle_t$ tilts positive and negative $\langle \tilde{\omega}_z \rangle_t$ for $y/H < 0$ and $y/H > 6$, respectively, explaining how the balance of these terms effectively eliminates their net contribution to extracrater $\langle \tilde{\omega}_x \rangle_t$ transport. In contrast, we have seen how spatial heterogeneity of the Reynolds stresses sustains the intracrater circulations, as sketched in Fig. 8 and shown in Fig. 6.

This extracrater mechanism of streamwise vorticity production is largely reproduced for case 4, shown in Fig. 7, where the stretching term [Figs. 7(a) and 7(b)] is an order of magnitude less than the tilting terms [Figs. 7(c)–7(f)]. Inside the crater, however, the physics change since the mound itself is now important to the production and sustenance of $\langle \tilde{\omega}_x \rangle_t$. Further, $\langle \tilde{\omega}_z \rangle_t$ is subjected to vortex stretching and compression at the two streamwise locations shown, owing to flow entering the crater basin and coursing laterally around the moat. Similarly, we can see that at $x/H = 6$ (right panels), the tilting of spanwise and vertical vorticity into the streamwise direction makes a roughly equal-and-opposite contribution

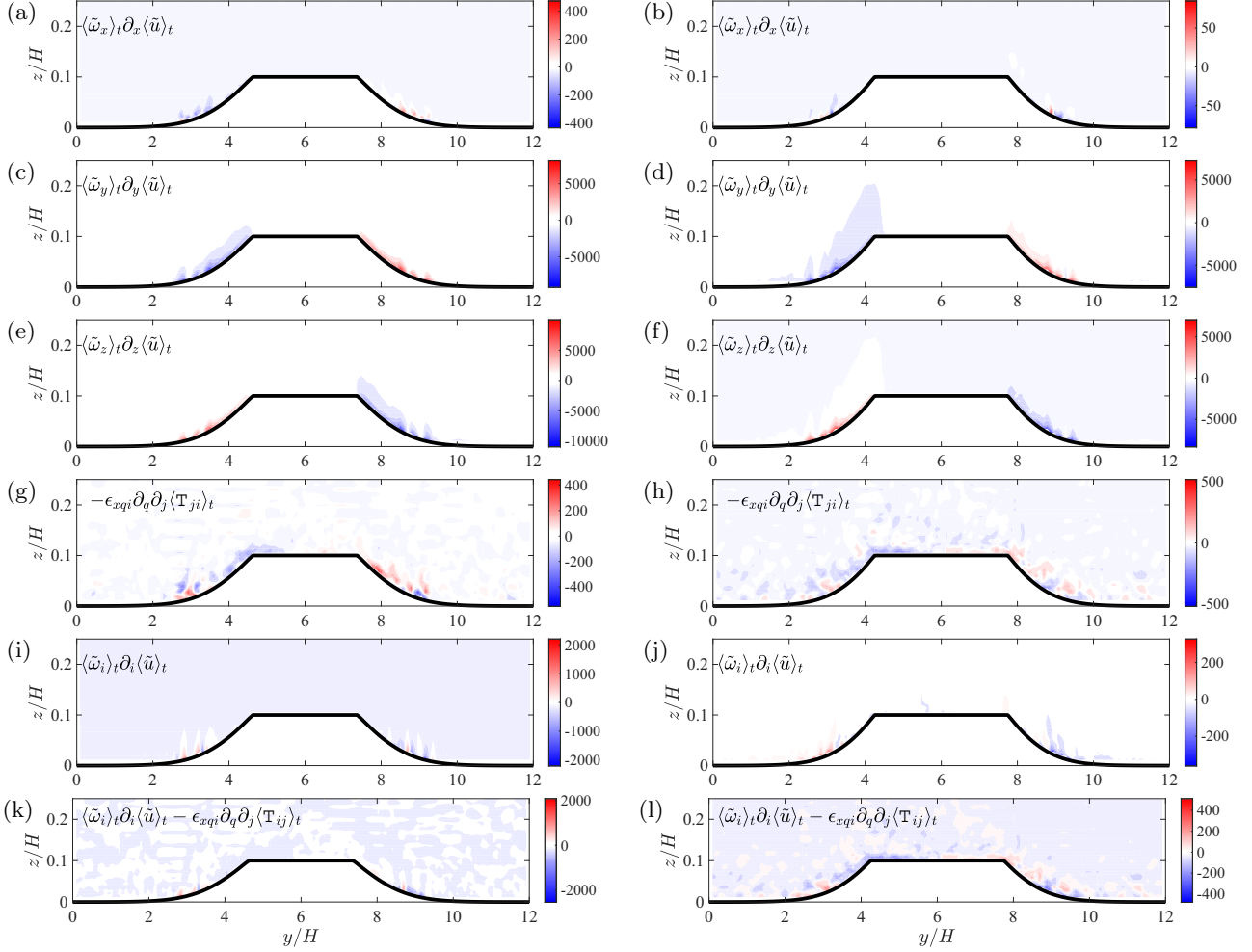


FIG. 7. Visualization of constituent terms from the Reynolds-averaged streamwise vorticity transport equation for flow over case 4 at streamwise positions $x/H \approx 5$ (left panels) and $x/H = 6$ (right panels) (see Fig. 1 for reference), showing (a) and (b) stretching of $\langle \tilde{\omega}_1 \rangle_t$ by $\partial_1 \langle \tilde{u}_1 \rangle_t$, (c) and (d) tilting of $\langle \tilde{\omega}_2 \rangle_t$ by $\partial_2 \langle \tilde{u}_1 \rangle_t$, (e) and (f) show tilting of $\langle \tilde{\omega}_3 \rangle_t$ by $\partial_3 \langle \tilde{u}_1 \rangle_t$, (g) and (h) production of $\langle \tilde{\omega}_1 \rangle_t$ by turbulent torque, (i) and (j) the sum of $\langle \tilde{\omega}_1 \rangle_t$ gain and loss via mean-flow gradients, and (k) and (l) the sum of terms contributing to the gain and loss of $\langle \tilde{\omega}_1 \rangle_t$.

to intracrater $\langle \tilde{\omega}_x \rangle_t$. Turbulent torque makes a significant contribution to $\langle \tilde{\omega}_x \rangle_t$ within the crater, as shown in Figs. 7(g) and 7(h). At $x/H \approx 5$ and 6, the turbulent torque spatial distribution is a clear driver of $\langle \tilde{\omega}_x \rangle_t$. At $x/H = 6$ [Fig. 7(h)], turbulent torque sustains two intracrater counterrotating helical vortices flanking the mound, observed as positive and negative at $y/H = 5$ and 7, respectively. There are two additional circulations aloft the basin, at elevation $z/H \approx 0.15$ and $y/H \approx 4.5$ and $y/H \approx 7.5$. These effects can be more readily visualized through the net right-hand side of Eq. (10), shown in Figs. 7(k) and 7(l). At $x/H \approx 5$, there is a predominant contribution to intracrater $\langle \tilde{\omega}_x \rangle_t < 0$ and $\langle \tilde{\omega}_x \rangle_t > 0$ at $y/H = 5.5$ and $y = 6.5$, respectively, due mainly to the stretching-and-tilting term [compare against Fig. 7(i)]. However, by $x/H = 6$, these counterrotating vortices have risen vertically and flank the crater rim ($\langle \tilde{\omega}_x \rangle_t < 0$ and $\langle \tilde{\omega}_x \rangle_t > 0$ at $y/H = 4.5$ and $y = 7.5$). At $x/H = 6$, the intracrater circulations are mainly turbulent secondary flows with $\langle \tilde{\omega}_x \rangle_t > 0$ and $\langle \tilde{\omega}_x \rangle_t < 0$ at $y/H = 5$ and $y = 7$.

The vorticity dynamics results for case 4 (Fig. 7) are conceptually supported by the Fig. 8 schematic, although sediment excavation of the moat creates a region for intracrater

circulations. Figure 8 shows the two intracrater circulations inferred for case 4, while the preceding study of helicity (Fig. 5 and accompanying text) shows that these counterrotating helical vortices are in motion and therefore are important to aeolian excavation of the crater fill. Previous articles on reconstructed intracrater winds from aeolian wind markers [11] demonstrate the influence of intracrater circulations as an aeolian excavation agent (in addition to the influence of katabatic winds [9,10]), but the underlying mechanisms responsible for sustaining these circulations have not received the same level of attention. In the following section, statistics of the flow at discrete locations are used to further the present study.

C. Probability density functions of time-series measurements

In Sec. III B, vorticity dynamics analysis of cases 1 and 4 crater flows (cases 2, 3, and 5 were not shown for brevity, although these cases exhibited similar trends) culminated in demonstrating how intracrater circulations primarily receive sustenance from the turbulent torque term. For intracrater aeolian morphodynamics, this result is significant since the scaling laws for mass fluxes via saltation Q and dust emissions F scale

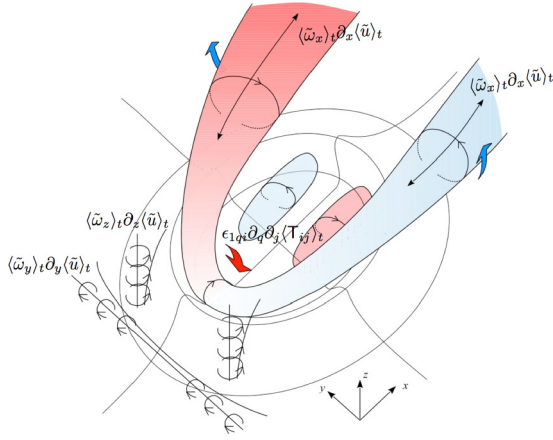


FIG. 8. Structural model of intracrater and extracrater secondary flows aloft an idealized synthetic crater, highlighting spatial locations wherein different mechanisms contribute towards gains and losses in mean streamwise vorticity. Preceding arguments lead us to conclude that tilting of vertical and spanwise vorticity is overwhelmingly responsible for streamwise vorticity upwind of the crater (denoted by black lines and annotations upwind of the rim), stretching of ambient streamwise vorticity is largest above the crater (red-blue contour), and turbulent torque is strongest within the crater (red-blue contour).

upon shear (aerodynamic) velocity u_τ to some exponents n and m , respectively [12,13,38,43,44]. The relations $Q \sim u_\tau^3$ and $F \sim u_\tau^4$ are commonly reported, illustrating the sensitivity of aeolian-dominated landscapes to even moderate increases in u_τ . We recognize that the precise value of the exponent in these scaling relations is an open question; in order to remain focused on the primary theme of this paper, we have used the standard values of $Q \sim u_\tau^3$ and $F \sim u_\tau^4$. For the intracrater circulations, sustained almost entirely by turbulence, it is thus of importance to consider statistical attributes of flow in the crater to quantify variability in u_τ -inducing fluctuations. In this section, we show probability density functions (PDFs) from discrete intracrater locations. These results are used to highlight the intermittent nature of turbulent fluctuations aloft the crater.

Figure 9 shows PDFs of fluctuating streamwise velocity (left panels) and vertical velocity (right panels) at discrete intracrater locations; see Fig. 2 for reference. The line coloring convention is defined in the caption. The discrete locations \mathbf{x}_2 , \mathbf{x}_3 , \mathbf{x}_4 , and \mathbf{x}_5 were selected since they are streamwise aligned and located at the spanwise center of the domain. Thus, statistics from location \mathbf{x}_2 are expected to be influenced by vortex shedding from the upwind rim, positions \mathbf{x}_3 and \mathbf{x}_4 are expected to be more heavily influenced by the moat and mound (if present), and \mathbf{x}_5 will be influenced by separation off the downwind rim.

The PDFs all exhibit wide variability, with $\tilde{u}'(\mathbf{x}_l, t)$ and $\tilde{w}'(\mathbf{x}_l, t)$ able to vary over an order of magnitude. Moreover, by selecting these locations, we can clearly demonstrate that the PDFs do not narrow at different locations (PDFs at other locations all exhibit a similarly wide variability, but were not shown here for brevity). In the preceding sections, we have considered visualization of either instantaneous (Fig. 3) or Reynolds-averaged (Figs. 4–7) quantities.

An alternative averaging approach that reveals the spatial attributes of turbulent structures present during high-magnitude low-frequency events is conditional averaging [37,38,45–50]. In this averaging approach, a threshold is set and the flow is sampled when the threshold is exceeded by a predefined quantity

$$\frac{\widehat{\tilde{u}}(\mathbf{x})}{u_\tau} = \left\langle \frac{\tilde{u}(\mathbf{x}, t)}{u_\tau} \middle| \alpha \geq \beta \right\rangle_{N_s}, \quad (11)$$

where a caret denotes a conditionally averaged quantity, α is the predefined quantity, β is the threshold, and N_s is the number of exceedances. In the following sections, we show results for conditionally sampling the flow via

$$\frac{\widehat{\tilde{u}}(\mathbf{x})}{u_\tau} = \left\langle \frac{\tilde{u}(\mathbf{x}, t)}{u_\tau} \middle| \frac{\tilde{u}'(\mathbf{x}_2, t)}{u_\tau} \geq 4 \right\rangle_{N_s}, \quad (12)$$

where the PDF of $\tilde{u}'(\mathbf{x}_2, t)/u_\tau$ and the threshold $\tilde{u}'(\mathbf{x}_2, t)/u_\tau = 4$ are shown in Fig. 9(a), for reference. The PDF shows that $p(\tilde{u}'(\mathbf{x}_2, t) > \beta) \approx 10^{-1}$; thus, the resultant $\widehat{\tilde{u}}(\mathbf{x})$ will reveal the spatial attributes of structures aloft the crater when the fluctuating velocity at \mathbf{x}_2 exceeds a value that occurs 10% of time. This is the kind of low-frequency high-magnitude event that is of primary importance to aeolian activity [38] in the low-density environment of Mars and its importance is reinforced by consideration of the scaling arguments already given for aeolian mass fluxes by saltation and dust emissions. Many sampling locations could have been selected, but we selected \mathbf{x}_2 for its location downwind of the rim and above the basin, where vortices shed from the rim begin to undergo spatial realignment via stretching, tilting, and turbulence, as outlined in Sec. III B.

D. Conditionally sampled flow

Equation (12) has been used to generate conditionally averaged velocity $\widehat{\tilde{u}}(\mathbf{x})/u_\tau$, from which we compute conditionally averaged vorticity $\widehat{\tilde{\omega}}(\mathbf{x})Hu_\tau^{-1} = \nabla \times \widehat{\tilde{u}}(\mathbf{x})Hu_\tau^{-1}$. Here we have elected to show results for cases 2 (initial basin depression), 4 (moat and mound), and 5 (empty crater). Results for other cases could certainly have been shown, and were computed, but for brevity are not included here.

Figure 10 shows isocontours of $\widehat{\tilde{\omega}}$. Figure 10(a) shows $\widehat{\tilde{\omega}}_y = \partial_z \widehat{\tilde{u}} - \partial_x \widehat{\tilde{w}}$, where the former term $\partial_z \widehat{\tilde{u}}$ makes the predominant contribution to $\widehat{\tilde{\omega}}_y$. Thus, Fig. 10(a) essentially demonstrates wall-normal shear, which scales linearly with surface momentum fluxes under the presumption of Boussinesq scaling [51] $\widehat{\tilde{\omega}}_y \approx \partial_z \widehat{\tilde{u}} \sim \mathbf{Q}_{xz}$, during persistent high-magnitude low-frequency events at \mathbf{x}_2 , where \mathbf{Q} is the component of the Reynolds stresses retained during conditional sampling. During these extreme high-momentum fluctuations at \mathbf{x}_2 , there is a region of elevated surface shear across the basin, in the region $5.5 \lesssim y/H \lesssim 6.5$ and $4.5 \lesssim x/H \lesssim 6$, flanked by two radial bands of elevated shear concentrated around the crater inner walls. The elevated shear across the basin is a product of high-magnitude sweeps associated with shedding of vortices from the crater rim, which will intermittently erode sediment between the rim and crater geometric center. The two radial bands flanking the crater rim for $x/H \lesssim 6$ are a product of high-magnitude winds aloft the rim.

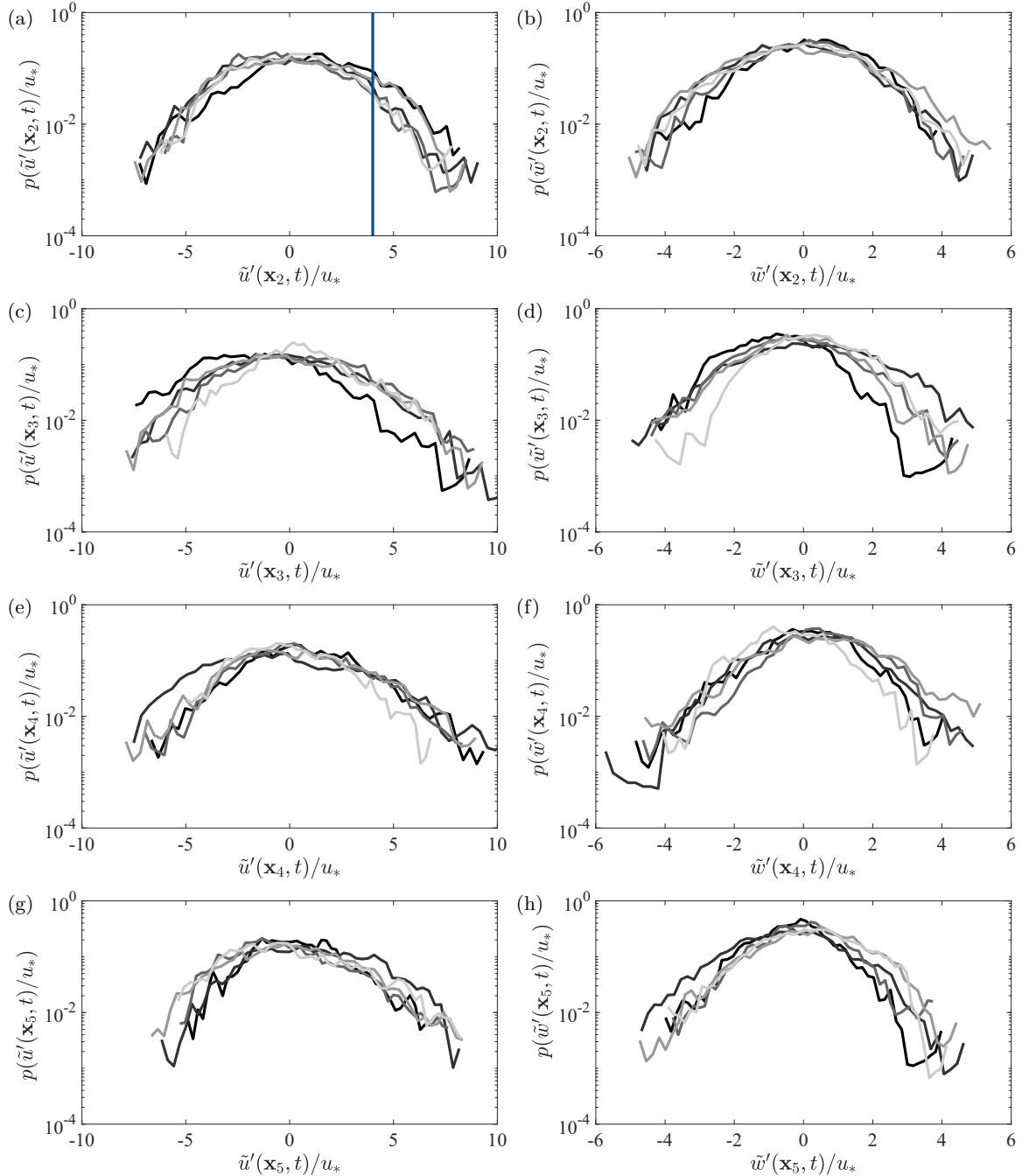


FIG. 9. Probability density functions of streamwise and vertical velocity fluctuations $\tilde{u}'(\mathbf{x}_l, t)$ (left panels) and $\tilde{w}'(\mathbf{x}_l, t)$ (right panels), from local positions \mathbf{x}_l throughout the domain (see also Fig. 2 for reference): (a) and (b) $\mathbf{x}_l = \mathbf{x}_2$, (c) and (d) $\mathbf{x}_l = \mathbf{x}_3$, (e) and (f) $\mathbf{x}_l = \mathbf{x}_4$, and (g) and (h) $\mathbf{x}_l = \mathbf{x}_5$. Panel (a) shows conditional sampling thresholds used in present study. Colors correspond to case 1 (black), case 2 (dark gray), case 3 (gray), case 4 (light gray), and case 5 (lightest gray). The vertical blue line in (a) illustrates the threshold used to conditionally sampled the flow.

Isocontours of positive and negative $\hat{\omega}_x$, shown in Fig. 10(b), reveal that the crater is flanked by two extracrater helical vortices. These are distinctly different to the intracrater vortices (Sec. III B) and structural model already hypothesized (Fig. 8). The results for case 2 suggest that the helical intracrater vortices did not play a major role in early recession of the sediment-filled basin. Instead, it was the shedding of vortices from the rim, realized in spanwise vorticity, and plunging air masses from aloft [Fig. 10(a)] that drove initial

recession of the basin. The helical intracrater vortices were, however, prevalent after the initial moat recession had begun, as shown in the isocontours for cases 4 and 5.

Figures 11 and 12 show isocontours of conditionally sampled spanwise [Figs. 11(a) and 12(a)] and streamwise [Figs. 11(b), 11(c), 12(b), and 12(c)] vorticity for cases 4 and 5, respectively. As per Fig. 10(a), isocontours of $\hat{\omega}_y$, a proxy for surface shear, are mainly concentrated around the crater upwind and downwind rim. A difference, however, is that

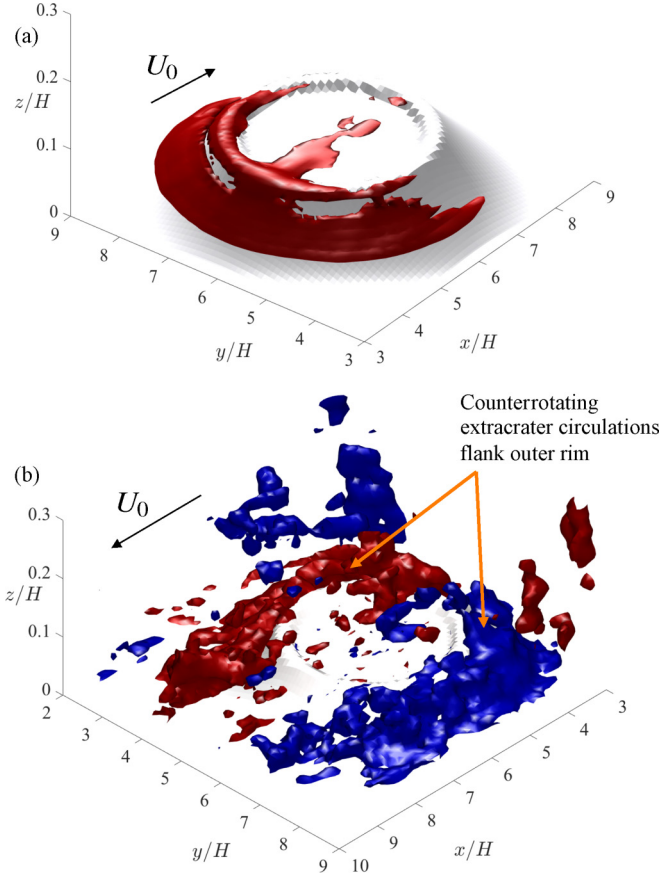


FIG. 10. Conditionally sampled vorticity from flow over case 2 (see also Fig. 2), with the conditional sampling threshold defined based on streamwise velocity fluctuations at location \mathbf{x}_2 , where a probability density function of this quantity has been provided in Fig. 9(a). (a) Spanwise vorticity $\widehat{\omega}_y$, and (b) streamwise vorticity $\widehat{\omega}_x$ are shown, with U_0 added to denote the main atmospheric flow direction (note also that the horizontal ranges of the panels have been varied to show as much information as possible on flow structures associated with the crater). Shown in (b) are $\widehat{\omega}_x$ contours for equal-and-opposite values of $\widehat{\omega}_x$ (red and blue are positive and negative, respectively), in order to reveal the counterrotating extracrater vortices flanking the rim.

for cases 4 and 5, the crater sedimentary fill is not available to absorb drag. Moreover, the isocontours of $\widehat{\omega}_x$ reveal that during high-magnitude low-frequency streamwise velocity fluctuations at \mathbf{x}_2 , the flow exhibits structural attributes similar to that presented in the Fig. 8 structural model.

Figure 11(b) reveals the presence of two intracrater counterrotating vortices with sign consistent with the Fig. 8 model. These two vortices are actively advected downwind, as supported by helicity visualizations (Fig. 5), and in so doing they abrade and erode sediment from the edges of the crater basin first, leaving the mound that is itself retreating downwind. These two vortices emanate from the crater basin, as is highlighted in the figure. These counterrotating circulations are present for case 5, too, although for this case the basin is now entirely empty. Note also that for case 4, two smaller counterrotating vortices occupy space downwind of the mound, as highlighted in Fig. 11(b). This is consistent with results in Sec. III B.

E. Inferred aerodynamic stresses from conditionally sampled flow

In order to further the analysis and fully attribute the aloft flow patterns with aeolian morphodynamics within the crater, we have used the Reynolds- and conditionally averaged flow aloft the crater to predict imposed surface (basal) stress. Since $\tau^w = \rho u_\tau^2$, it follows that $Q \sim (\tau^w)^{3/2}$ and $F \sim (\tau^w)^2$ [12,44], which demonstrates how brief deviations from the mean could induce high mass fluxes. Also, as reviewed in Secs. III C and III D, turbulent fluctuations are strong everywhere in the crater and are in fact responsible for sustenance of the secondary vortical flows (Sec. III B).

The Reynolds- and conditionally averaged surface stress distributions are computed *a posteriori* by first retrieving the isoelevation velocity at fixed height $\zeta(x, y) = \Delta_z + h(x, y)$. In the present simulations where $H = 10\,000$ m and $N_z = 128$, $\Delta_z \approx 80$ m, although we reemphasize that all quantities are nondimensionalized in LES (see Sec. II). Since $\zeta(x, y) = \delta_z + h(x, y)$ is not colocated with grid points on the computational mesh, $\langle \tilde{\mathbf{u}} \rangle_t(\mathbf{x})$ and $\widehat{\mathbf{u}}(\mathbf{x})$ must be locally interpolated to attain $\langle \tilde{\mathbf{u}} \rangle_t(x, y, \zeta(x, y))$ and $\widehat{\mathbf{u}}(x, y, \zeta(x, y))$. Once this interpolation has been completed, $\langle \tilde{\mathbf{u}} \rangle_t(x, y, \zeta(x, y))$ and $\widehat{\mathbf{u}}(x, y, \zeta(x, y))$ can be substituted into the equilibrium wall model (3). For the Reynolds-averaged flow, substitution yields

$$\frac{\langle \tau_{iz}^{\zeta, w} \rangle_t(x, y)}{\rho u_\tau^2(x, y)} = - \left[\frac{\kappa \langle U \rangle_t(x, y, \zeta(x, y))}{\ln(\Delta_z/z_0)} \right]^2 \frac{\langle \tilde{u}_i \rangle_t(x, y, \zeta(x, y))}{\langle U \rangle_t(x, y, \zeta(x, y))}, \quad (13)$$

where $i = 1$ and 2 , $\langle U \rangle_t(x, y, \zeta(x, y)) = (\langle \tilde{u}^2(x, y, \zeta(x, y)) \rangle_t + \langle \tilde{v}^2(x, y, \zeta(x, y)) \rangle_t)^{1/2}$, and the superscript ζ on surface stress denotes isoelevation. For the conditionally sampled flow, substitution yields

$$\frac{\widehat{\tau}_{iz}^{\zeta, w}(x, y)}{\rho u_\tau^2(x, y)} = - \left[\frac{\kappa \widehat{U}(x, y, \zeta(x, y))}{\ln(\Delta_z/z_0)} \right]^2 \frac{\widehat{u}_i(x, y, \zeta(x, y))}{\widehat{U}(x, y, \zeta(x, y))}, \quad (14)$$

where $i = 1$ and 2 , $\widehat{U}(x, y, \zeta(x, y)) = [\widehat{u}^2(x, y, \zeta(x, y)) + \widehat{v}^2(x, y, \zeta(x, y))]^{1/2}$, and the superscript ζ on surface stress, as above, denotes isoelevation. In order to illuminate differences in the spatial distributions between $\langle \tau_{xz}^{\zeta, w} \rangle_t(x, y)/\rho u_\tau^2(x, y)$ and $\widehat{\tau}_{xz}^{\zeta, w}(x, y)/\rho u_\tau^2(x, y)$, the former is subtracted from the latter before visualization:

$$\frac{\widehat{\tau}_{xz}^{\zeta, w'}(x, y)}{\rho u_\tau^2(x, y)} = \frac{\widehat{\tau}_{xz}^{\zeta, w}(x, y)}{\rho u_\tau^2(x, y)} - \frac{\langle \tau_{xz}^{\zeta, w} \rangle_t(x, y)}{\rho u_\tau^2(x, y)}. \quad (15)$$

For the present discussion, we consider only $\langle \tau_{xz}^{\zeta, w} \rangle_t(x, y)/\rho u_\tau^2(x, y)$ and $\widehat{\tau}_{xz}^{\zeta, w'}(x, y)/\rho u_\tau^2(x, y)$ and do not present results for the spanwise-wall-normal surface stresses [$\langle \tau_{yz}^{\zeta, w} \rangle_t(x, y)/\rho u_\tau^2(x, y)$ and $\widehat{\tau}_{yz}^{\zeta, w'}(x, y)/\rho u_\tau^2(x, y)$]. The streamwise-wall-normal component of surface stress absorbs the overwhelming majority of turbulent momentum fluxes since this direction balances the imposed atmospheric pressure gradient Π in Eq. (1). Although the crater induces secondary flows that develop some finite values of spanwise-wall-normal stress, the greatest values (and therefore the most relevant for aeolian erosion) are driven by the streamwise-wall-normal component.

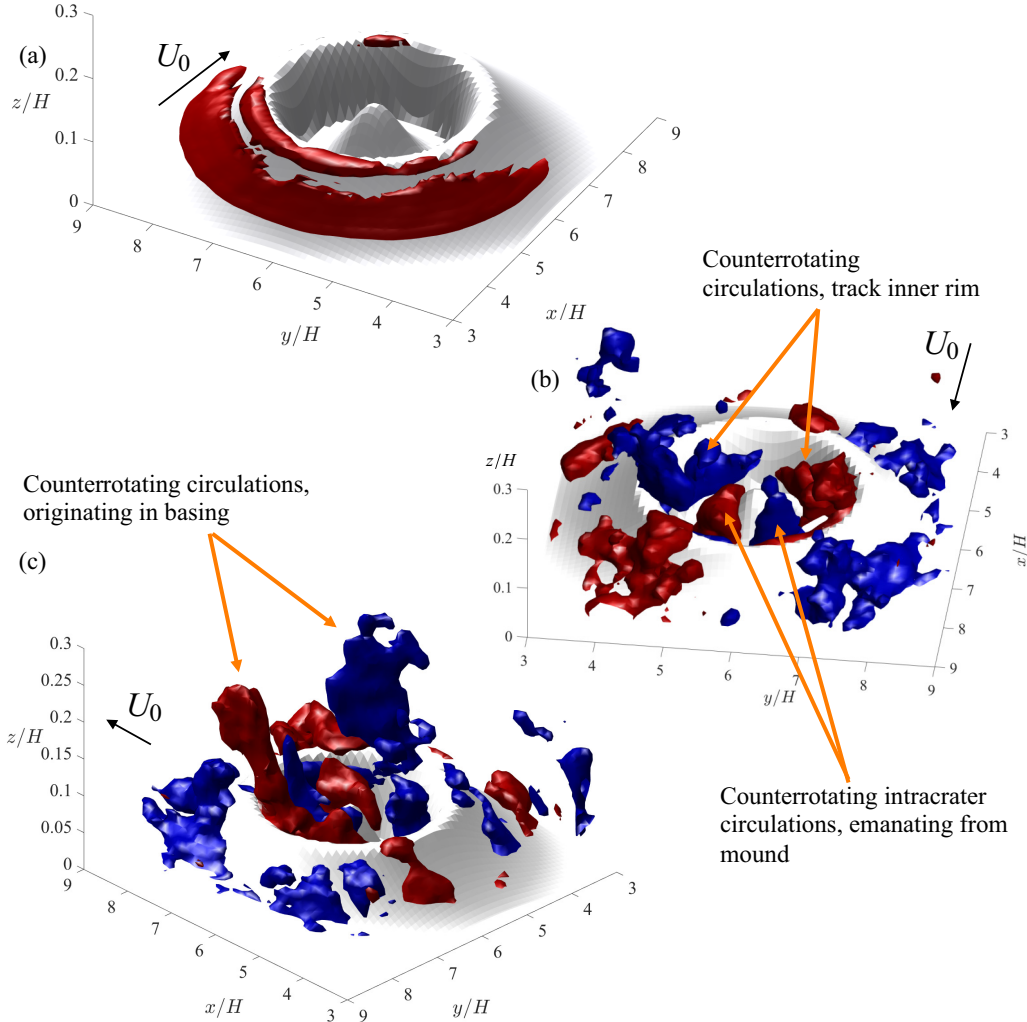


FIG. 11. Conditionally sampled spanwise vorticity from flow over case 4 (see also Fig. 2), with the conditional sampling threshold defined based on streamwise velocity fluctuations at location x_2 , where a probability density function of this quantity has been provided in Fig. 9(a). (a) Spanwise vorticity $\hat{\omega}_y$ and (b) streamwise vorticity $\hat{\omega}_x$ are shown from (b) and (c) two visualization perspectives, with U_0 added to denote the main atmospheric flow direction (note also that the horizontal ranges of the panels have been varied to show as much information as possible on flow structures associated with the crater). Shown in (b) and (c) are $\hat{\omega}_x$ contours for equal-and-opposite values of $\hat{\omega}_x$ (red and blue are positive and negative, respectively), in order to reveal the counterrotating extracrater vortices flanking the rim.

Figure 13 presents Reynolds- and conditionally averaged isoelevation velocity for cases 1 and 4, respectively, as described in the accompanying figure caption. The figure also shows the corresponding Reynolds-averaged surface stress distribution as per Eq. (13) [Figs. 13(c) and 13(g)], while Figs. 13(d) and 13(h) illustrate the conditionally averaged stress, as computed with Eqs. (14) and (15).

Figures 13(a) and 13(e) show $\langle \tilde{u} \rangle_t(x, y, \zeta(x, y))$ for cases 1 and 4, respectively. The color bars indicate that darker colors correspond to higher $\langle \tilde{u} \rangle_t(x, y, \zeta(x, y))$. Beginning first with case 1, Fig. 13(a) shows that the flow aloft the basin is characterized by a series of crescentlike bands of $\langle \tilde{u} \rangle_t(x, y, \zeta(x, y))$, where the magnitude of each decreases in the downwind direction. These bands of elevated $\langle \tilde{u} \rangle_t(x, y, \zeta(x, y))$ are highest around the edge of the basin and are attributed to lateral steering of flow at the upwindmost point of the crater, which is then forced upward over the crater walls. This pattern of elevated bands of $\langle \tilde{u} \rangle_t(x, y, \zeta(x, y))$ around

the edges of the basin can be attributed to the initiation of moat excavation [8]. However, these bands alone would erode only lateral crescentic recessions, while the central region, $4.5 \lesssim x/H \lesssim 6$ and $5.5 \lesssim y/H \lesssim 6.5$, the future upwind site of a mound, would remain unaffected. This conclusion can also be deduced from consideration of the Reynolds-averaged surface stresses [Eq. (13) and Fig. 13(c)], which shows a similar pattern of symmetric bands of elevated stress across the edges of the basin. However, the PDFs have already shown that flow, and therefore stress, aloft the basin exhibits a wide variability owing to turbulent fluctuations. Indeed, conditionally averaged vorticity isocontours revealed the presence of large coherent rollers during the occurrence of low-probability high-magnitude events.

Figure 13(b) shows the conditionally sampled streamwise velocity, less the Reynolds-averaged streamwise velocity $\hat{u}' = \hat{u} - \langle \tilde{u} \rangle_t$. Removal of the Reynolds-averaged streamwise velocity helps to reveal where the affects of turbulent fluctuations

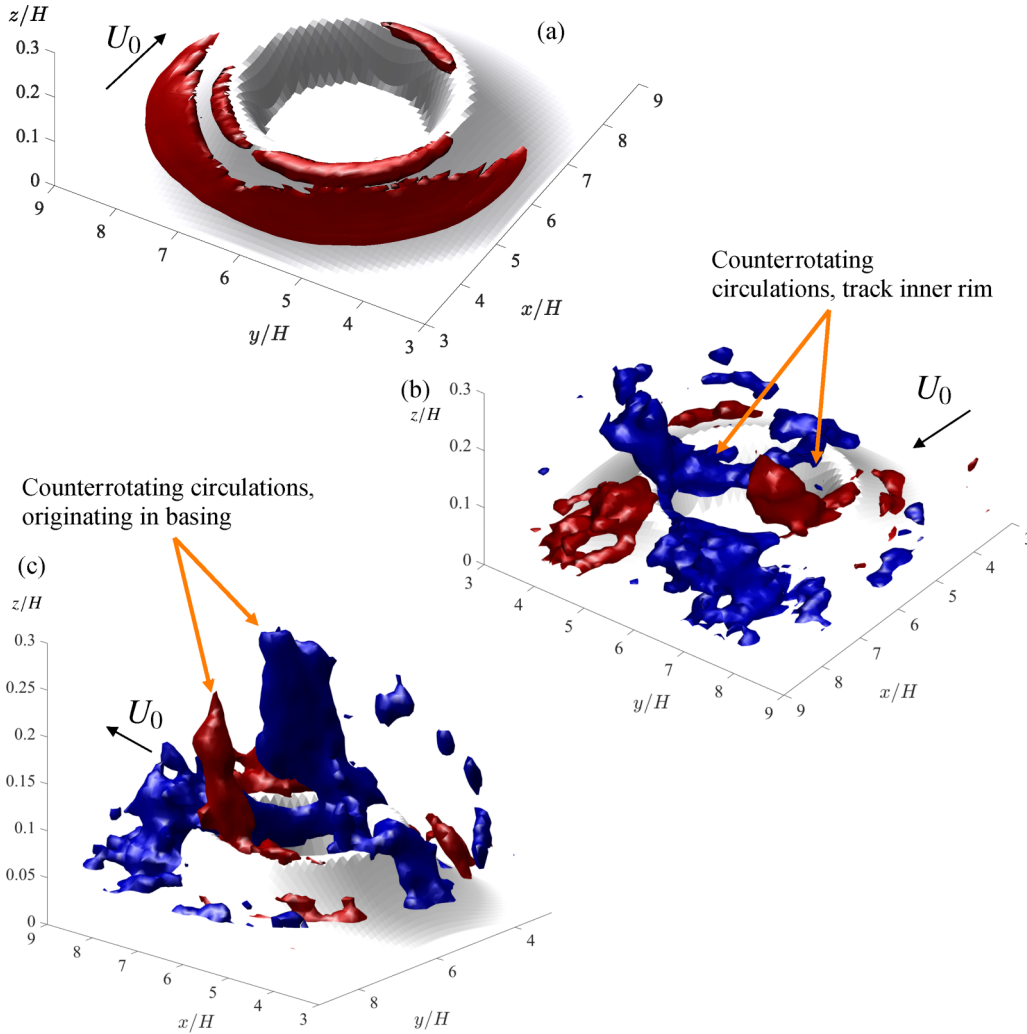


FIG. 12. Conditionally sampled spanwise vorticity from flow over case 5 (see also Fig. 2), with the conditional sampling threshold defined based on streamwise velocity fluctuations at location x_2 , where a probability density function of this quantity has been provided in Fig. 9(a). (a) Spanwise vorticity $\hat{\omega}_y$ and (b) streamwise vorticity $\hat{\omega}_x$ are shown from (b) and (c) two visualization perspectives, with U_0 added to denote the main atmospheric flow direction (note also that the horizontal ranges of the panels have been varied to show as much information as possible on flow structures associated with the crater). Shown in (b) and (c) are $\hat{\omega}_x$ contours for equal-and-opposite values of $\hat{\omega}_x$ (red and blue are positive and negative, respectively), in order to reveal the counterrotating extracrater vortices flanking the rim.

at x_2 are most pronounced. Indeed, this procedure reveals a region of elevated \hat{u}' immediately upwind of the sampling point, due to the high-magnitude fluctuations as eddies are shed from the rim. Indeed, the signature of this \hat{u}' distribution can also be discerned from the $\hat{\omega}_y(x)$ isocontours in Fig. 10(a): The intermittent, but dramatic, shedding of eddies from the upwind rim manifests as a parcel of high shear across the rim and immediately upwind of the sampling point. Figure 13(d) shows the corresponding distribution of $\log[|\hat{\tau}_{yz}^{\zeta, w'}(x, y)/\rho u_\tau^2(x, y)|]$ [Eq. (15)], which is spatially consistent with the Fig. 13(b) result, but different from the Reynolds-averaged surface stress shown in Fig. 13(c).

The $\log[|\hat{\tau}_{yz}^{\zeta, w'}(x, y)/\rho u_\tau^2(x, y)|]$ distribution displays a prominent region of elevated stress in close proximity to the sampling point. The results presented in Figs. 13(c) and 13(d) provide insight into the processes responsible for initiating erosion of the moat and thus carving of the mound. The mean flow, by itself, would certainly excavate lateral recessions, but

would not induce substantial erosion in the region between the most upwind point of the rim and the basin geometric center. Simultaneously occurring turbulent fluctuations, however, would erode sediment precisely from this point, helping to sustain a crescent-shaped trough that gradually deepens. Kite *et al.* [9,10] have proposed katabatic winds as a depositional mechanism by which sedimentary mounds could have grown in craters and suggested that some later erosion by katabatic winds may have affected these mounds as well. However, in a filled crater basin not enough relief would exist for katabatic winds to drive the erosion needed to create the observed mound morphologies. We emphasize that wind tunnel observations by Day *et al.* [8] also reported this crescent-shaped landscape retreat.

Initial erosion of the crescentic recession, precursor to the formation of a full radial moat, creates a geometry that has an inherent feedback on the flow. The five synthetic craters were designed to capture five stages of moat deepening. In

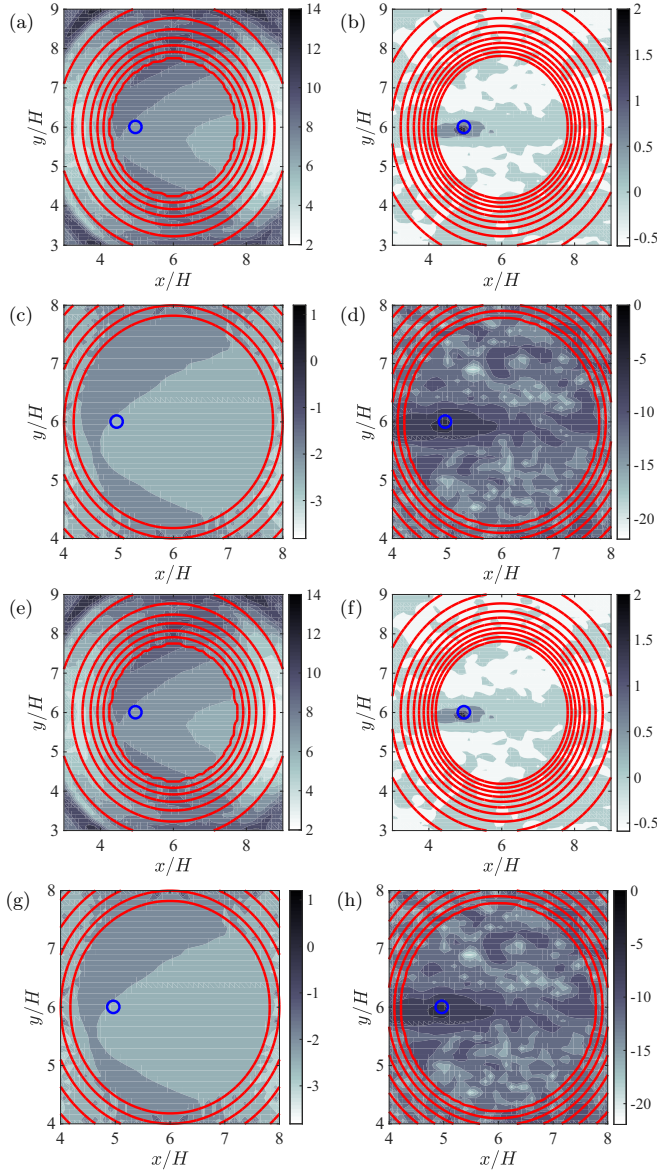


FIG. 13. (a), (b), (e), and (f) Interpolated isoelevation velocity and (c), (d), (g), and (h) corresponding surface stress for (a), (c), (e), and (g) Reynolds-averaged and (b), (d), (f), and (h) conditionally sampled flow over (a)–(d) case 1 and (e)–(h) case 2 craters, showing (b) and (f) fluctuation about the Reynolds average $\hat{u} - \langle \tilde{u} \rangle_t$, (c) and (g) surface stress computed with Eq. (13), and (d) and (h) surface stress computed with Eq. (15). Note that Panels (c) and (g) are $\log[|\langle \tau_{yz}^{\zeta,w} \rangle_t(x,y)/\rho u_\tau^2(x,y)|]$ and (d) and (h) are $\log[|\hat{\tau}_{yz}^{\zeta,w}(x,y)/\rho u_\tau^2(x,y)|]$, where the logarithm helps to reveal spatial variability of surface stress. Solid red lines denote $h(x,y)$. The sampling point x_2 , illustrated in Fig. 2, is marked with a blue circle; the PDF of $\tilde{u}(x_2, t)$ and the sampling threshold are shown in Fig. 9(a).

the interest of brevity, we do not show isoelevation velocity and stress for case 2, since this case closely resembles case 1. Similarly, cases 3 and 4 are somewhat similar, while case 5 (empty crater) is attained following total erosion of the moat and mound. Therefore, we show isoelevation velocity and stress for case 4 only.

Figure 13(e) shows $\langle \tilde{u} \rangle_t(x, y, \zeta(x, y))$ for case 4, where the red topographic lines are added to associate the flow patterns

and crater geometry. It is clear that flow is forced to accelerate in the space between the mound and adjacent walls, as inferred from the zones of elevated $\langle \tilde{u} \rangle_t(x, y, \zeta(x, y))$ over the region $5.5 \lesssim x/H \lesssim 7$ and on adjacent sides of the mound. This distribution directly affects surface stress, shown in Fig. 13(g). The surface stress distribution agrees closely with velocity, as would be expected, and exhibits large values on adjacent sides of the mound. Since case 4 has a clear moat, further erosion of this case will deepen the moat, erode the mound, and eventually empty the crater. Note, however, that the Reynolds-averaged velocity and stress [Figs. 13(e) and 13(g)] do not appear to greatly impact the windward face of the mound. This is similar to the results for case 1 [Figs. 13(a) and 13(b)].

The conditionally averaged streamwise velocity \hat{u}' for case 4 is shown in Fig. 13(f). Like case 1, it is clear that \hat{u}' exhibits large values beneath and upwind of the sampling point and the resultant $\log[|\hat{\tau}_{yz}^{\zeta,w'}(x,y)/\rho u_\tau^2(x,y)|]$ demonstrates that fluctuations are mainly responsible for erosion of the mound itself. This result also helps to explain the noted radial asymmetry of the mounds relative to the surrounding crater perimeter, as reviewed by Bennett and Bell [4].

F. Deflationary trajectory

The preceding results showed how turbulence is prevalent within the craters and in fact provides sustenance for the counterrotating helical vortices, while PDFs demonstrated the wide variability of velocity fluctuations from discrete locations aloft the crater basin. These findings were used to conditionally sample the flow, which revealed the spatial nature of the counterrotating intracrater vortices. The results in Sec. III E and Fig. 13 have been used here to summarize the likely deflationary trajectory of mid-latitude craters on Mars that were filled in the early history of Mars. It was shown that the Reynolds-averaged flow is responsible for lateral excavation of two streamwise-symmetric recessions, while fluctuations associated with vortex shedding and high-magnitude gusts are responsible for excavating mass from the region between the upwind rim and basin geometric center. Integrated forward in time, these two processed gradually empty the basin via formation of a crescentic depression, which retreats downwind in time while also deepening, before connecting at the downwind limit of the basin. The process has been sketched in Fig. 14.

In Fig. 14, arrows show two vortex lines (lines everywhere tangent to the vorticity vector) colored by streamwise vorticity. These lines are supported by the visualizations in Secs. III A and III B of helicity and vorticity isocontours, respectively. It would be speculative to associate times with the deflationary states illustrated in Fig. 14, since sediment and dust mass fluxes depend on atmospheric density. Nonetheless, the figure does summarize the wind tunnel observations of Day *et al.* [8] and the results reported throughout. Retreat of the crescentic recession will continue from the states reported in Figs. 8(e) and 8(f), resulting in an isolated mound, while the mound itself will eventually retreat, leaving an empty basin.

G. Wavelet power spectrum and global wavelet power spectrum

In this section, we present results of wavelet decomposition of the fluctuating velocity time series considered in Sec. III C.

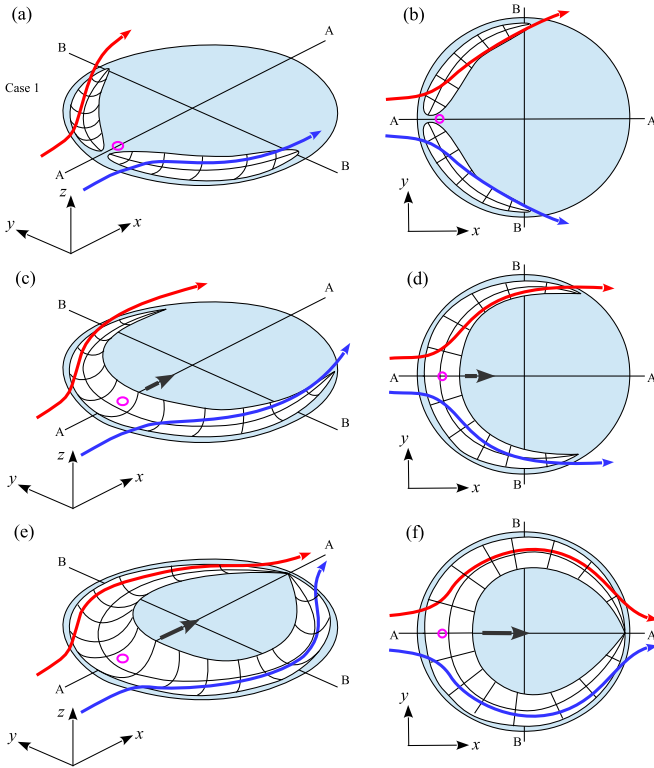


FIG. 14. Illustration of the deflationary trajectory of once-filled craters, showing (a), (c), and (e) perspective visualization, (b), (d), and (f) planform visualization, and (a) and (b) inferred deflation from case 1, representing (c) and (d) an inferred intermediate case and (e) and (f) configurations most similar to cases 3 and 4. Circle denotes the conditional sampling location \mathbf{x}_2 (see also Fig. 2) and arrows show vortex lines, colored by the local streamwise vorticity (where blue and red correspond to negative and positive $\langle \tilde{\omega}_x \rangle_t$, respectively).

Wavelet decomposition quantifies spectral density across constituent frequencies of the input signal [52,53], in this case $\tilde{u}'(\mathbf{x}_2, t)$ and $\tilde{w}'(\mathbf{x}_2, t)$. The analysis is predicated upon convolution of $\tilde{u}'(\mathbf{x}_2, t)$ and $\tilde{w}'(\mathbf{x}_2, t)$ with a wavelet (basis) function $\psi(f)$, which yields an array of coefficients in joint time-frequency space. The square of the absolute value of the wavelet coefficients, divided by each frequency, yields spectral density defined in time-frequency space $E_{\tilde{u}'\tilde{u}'}(\mathbf{x}_1, t) f U_0^{-3}$ and $E_{\tilde{w}'\tilde{w}'}(\mathbf{x}_1, t) f U_0^{-3}$, otherwise known as wavelet power spectrum contours. For the present work, we have used Morlet wavelets $\psi(t/t_s) = \exp(i\omega_\psi t/t_s) \exp(-|t/t_s|^2 \frac{1}{2})$, where we have chosen the relatively common nondimensional frequency, $|\omega_\psi| = 6$, t_s is the wavelet time scale, t is physical time, and i is the imaginary unit.

Figures 15(c) and 15(d) show input time series $\tilde{u}'(\mathbf{x}_3, t)$ and $\tilde{w}'(\mathbf{x}_3, t)$, respectively, for case 1, while Figs. 15(g) and 15(h) show input time series $\tilde{u}'(\mathbf{x}_3, t)$ and $\tilde{w}'(\mathbf{x}_3, t)$, respectively, for case 3. Inspection of the time series, by itself, does not reveal the signature of persistent perturbations that can be attributed to details of the geometry, nor does evaluation of the Fig. 9 PDFs. Yet, at \mathbf{x}_2 (and throughout), heretofore arguments have claimed that vortex shedding and turbulent mixing are of pivotal importance to moat erosion. Wavelet decomposition, however, provides a frequency-by-frequency

depiction of spectral density and is powerful for the present applications since the signature of salient crater geometric attributes may not impart broadband effects on the resultant time series.

Figures 15(a) and 15(b) show the result wavelet power spectrum contour for streamwise and vertical velocities, respectively, for case 1. Figures 15(e) and 15(f) show the result wavelet power spectrum contour for streamwise and vertical velocities, respectively, for case 3. In order to succinctly display differences in the wavelet power spectrum contours for case 1 to 5 craters, we have compiled profiles of the global wavelet power spectrum $\langle E_{\tilde{u}'\tilde{u}'}(\mathbf{x}_2, t) \rangle_t f U_0^{-3}$ and $\langle E_{\tilde{w}'\tilde{w}'}(\mathbf{x}_2, t) \rangle_t f U_0^{-3}$ in Figs. 16(a) and 16(b), respectively.

The profiles of $\langle E_{\tilde{u}'\tilde{u}'}(\mathbf{x}_2, t) \rangle_t f U_0^{-3}$ and $\langle E_{\tilde{w}'\tilde{w}'}(\mathbf{x}_2, t) \rangle_t f U_0^{-3}$ illustrate the spectral density of the input signals in frequency space. Both profiles exhibit a distinct peak at shear-normalized frequency $f H U_0^{-1} \approx 2$. Thus, in the time series of $\tilde{u}'(\mathbf{x}_2, t)$ and $\tilde{w}'(\mathbf{x}_2, t)$, the greatest energy resides at $f H U_0^{-1} = 2$. We introduce the high-Reynolds-number Strouhal number $St = f(UL^{-1}) \approx 0.25$, which is the nondimensional frequency at which vortices are shed from a bluff body of scale L subjected to an incoming flow with velocity U . In the present discussion, $U \rightarrow \langle \tilde{u}(\mathbf{u}_2, t) \rangle_t$ and L can be attributed to characteristics of the crater geometry. An obvious length scale for vortex shedding of the craters would be the crater height. Setting $L \rightarrow h$ and then shear normalizing the frequency, we attain $f H \langle \tilde{u}(\mathbf{u}_2, t) \rangle_t^{-1} = St H / h$, which is denoted by the blue band in Figs. 16(a) and 16(b). In fact, we have used a range of L values smaller and larger than h , since the outer wall of the crater exhibits a very gentle relief. Nonetheless, it is clear that the dominant energy storage at this frequency can be attributed to shedding of vortices from the rim.

Further, $\langle E_{\tilde{u}'\tilde{u}'}(\mathbf{x}_2, t) \rangle_t f U_0^{-3}$ exhibits a second peak at $f H U_0^{-1} = 2 \times 10^{-1}$, but only for cases 3–5, the cases with a significant moat. This somewhat surprising result can be quickly understood by computing a second high-Reynolds-number Strouhal number $f H \langle \tilde{u}(\mathbf{u}_2, t) \rangle_t^{-1} = St H / (D/2)$, where D is the crater diameter. That is, the spectral density exhibits a second peak that is smaller, but non-negligible, at a shear-normalized frequency derived from the high-Reynolds-number Strouhal number and half the crater diameter. This is the signature of intracrater circulations that cannot physically exist for cases 1 and 2 due to the presence of crater fill. Interestingly, the profile for $\langle E_{\tilde{w}'\tilde{w}'}(\mathbf{x}_2, t) \rangle_t f U_0^{-3}$ does not exhibit a distinct second peak, at least not at \mathbf{x}_2 . We attribute this to the structure of the recirculating eddies, which are mainly defined by streamwise velocity at the sampling point.

H. Deflationary progression

The antecedent results have comprehensively explored the nature and physics of intracrater turbulence, which culminated in a structural model for the aloft circulations (Fig. 8) and a candidate model for the deflationary trajectory (Fig. 14). These results have not, however, addressed the following question: *Could* intracrater winds have excavated the filled crater over a time scale between the Noachian-Hesperian boundary until the present? In order to leverage the preceding results to provide

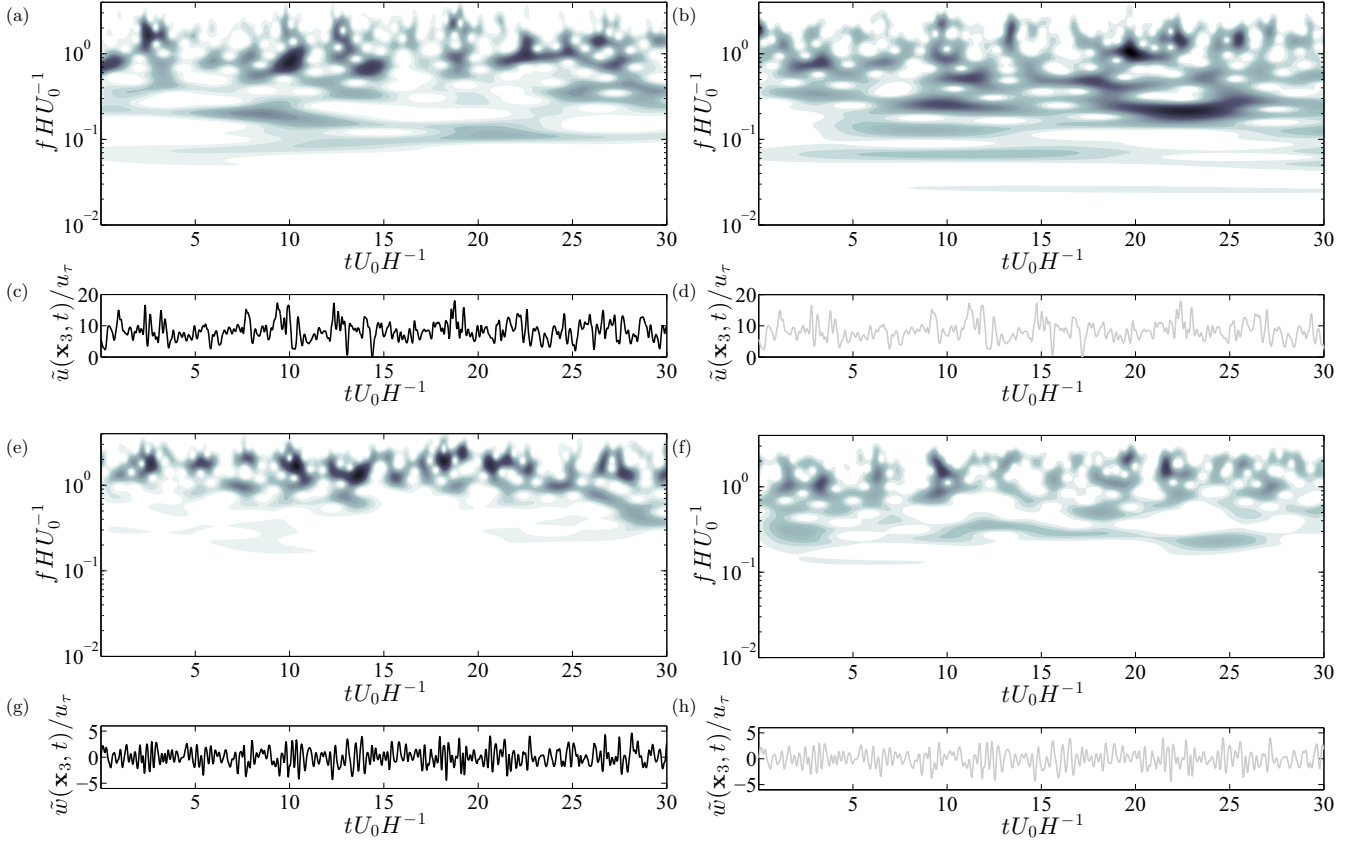


FIG. 15. Time-series processing of fluctuating (a)–(d) streamwise and (e)–(h) vertical velocity for case 1 (left panels) and case 3 (right panels), recorded at location \mathbf{x}_3 [see Figs. 2(c) and 2(d) for reference], showing (c), (d), (g), and (h) input time series and (a), (b), (e), and (f) the corresponding wavelet power spectrum contours $E_{\tilde{u}\tilde{u}'}(\mathbf{x}_3, t)fU_0^{-3}$ and $E_{\tilde{w}\tilde{w}'}(\mathbf{x}_3, t)fU_0^{-3}$, with outer-normalized frequency to facilitate introduction of Strouhal number St (i.e., $fHU_0^{-1} = St$). Note that time-series colors are consistent with the profile colors used in Figs. 9 and 16 (i.e., black and gray for cases 1 and 3, respectively).

rudimentary guidance on this question, we have performed a mass-balance analysis for a model of the crater fill and used established models for mass fluxes via saltation and dust emission. Consider a control volume encompassing the entire sedimentary fill present at the Noachian-Hesperian boundary

$$\frac{Dm_{CV}}{Dt} = \frac{\partial}{\partial t} \int_{\mathcal{V}} \rho_s d\mathcal{V} + \int_{\mathcal{A}} \rho_s \mathbf{u} \cdot \hat{\mathbf{n}} dA, \quad (16)$$

where m_{CV} is mass within the control volume, \mathcal{V} and \mathcal{A} denote the control volume and control surface area, respectively, ρ_s is

the sediment density, and the first and second right-hand side terms are the rate of change within the control volume and mass flux rate across the control surface, respectively, where \mathbf{u} is the local velocity field across \mathcal{A} , while $\hat{\mathbf{n}}$ is the local unit normal vector. This relation demonstrates the intrinsic dependence on the rate of mass excavation upon the flow field. Moreover, since mass is a conserved quantity, $Dm_{CV}/Dt = 0$ and Eq. (16) confirms that mass within the control must be decreasing while excavation is progressing. Assuming that $\rho_s(\mathbf{x}, t) \rightarrow \rho_s$ and following substitution of models for mass flux of sand (saltation) [43,44,54] and dust [12,13,44], Eq. (16) becomes

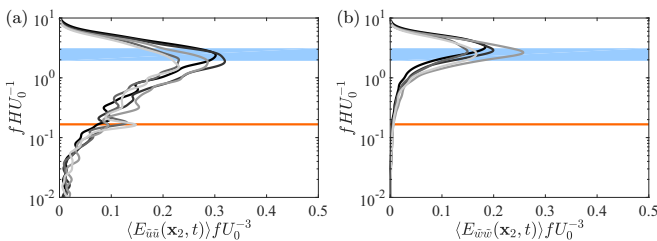


FIG. 16. Global wavelet power spectrum of (a) streamwise $\langle E_{\tilde{u}\tilde{u}'}(\mathbf{x}_2, t) \rangle_t fU_0^{-3}$ and (b) vertical $\langle E_{\tilde{w}\tilde{w}'}(\mathbf{x}_2, t) \rangle_t fU_0^{-3}$ velocity. The blue band denotes the shear-normalized frequency $fHU_0^{-1} = StH/L$, where $L \approx h$. The orange line denotes $fHU_0^{-1} = StH/L$, where $L \approx D/2$. Line colors correspond to case 1, black; case 2, dark gray; case 3, gray; case 4, light gray; and case 5, lightest gray.

$$\begin{aligned} & \frac{\rho_s}{\delta t} \int_r \int_{\theta} [h_f(r, \theta) - h_i(r, \theta)] r dr d\theta \\ & = \int_0^{\pi} QR d\theta + \int_0^R \int_0^{2\pi} Fr dr d\theta, \end{aligned} \quad (17)$$

where we have recast the equations in cylindrical coordinates for convenience of discussion. The first and second terms on the right-hand side represent mass egress from the crater via saltation Q ($=M^1L^{-1}T^{-1}$) and dust flux F ($=M^1L^{-2}T^{-1}$). Wind-driven mobilization of grains via saltation enables dust emissions; thus, in Eq. (17), we integrate F over the crater basin area, while integrating Q only over the downwind rim (assuming that saltating grains egress the crater only over this region of the rim). Saltation mass flux is modeled, for the

present discussion, using the Owen [54] model

$$Q = C \frac{\rho}{g} u_\tau^3 \left(1 - \frac{u_{\tau,t}^2}{u_\tau^2} \right), \quad (18)$$

where $C \sim O(10^0)$, ρ is atmospheric density on Mars, $g = 3.7 \text{ m s}^{-2}$ is gravitational acceleration on Mars, u_τ is ambient shear velocity developed via atmospheric pressure gradients (i.e., $u_\tau = (\tau^w/\rho)^{1/2} = ([dP_0/dx][H/\rho])^{1/2}$, where τ^w is imposed surface stress, dP_0/dx is atmospheric pressure gradient, and H is planetary boundary layer depth), and $u_{\tau,t}$ is threshold shear velocity [43]. The parenthetical term in Eq. (18) is a control that preserves $Q \geq 0$. There are numerous models for Q [12], but Eq. (18) is sufficient for the present cursory analysis. Models for dust emissions are typically predicated upon Q and we have adopted

$$F = \alpha Q, \quad (19)$$

after Gillette and Passi [55] and Marticorena and Bergametti [56], where $\alpha \sim O(10^{-5}-10^{-2})$ is the so-called sandblasting efficiency. With these models, we return to Eq. (17):

$$\frac{1}{\delta t} \rho_s \delta \mathcal{V} = Q\pi(D/2) + \alpha Q\pi(D^2/4), \quad (20)$$

where $\delta \mathcal{V}$ is the volume of eroded sedimentary rock since the Noachian-Hesperian boundary. This equation can be rearranged once more to attain a relation for the time required to excavate $\delta \mathcal{V}$ under representative conditions in the planetary boundary layer of Mars:

$$\delta t = \frac{\rho_s \delta \mathcal{V}}{Q\pi(D/2) + \alpha Q\pi(D^2/4)}. \quad (21)$$

The volume $\delta \mathcal{V}$ could be found with precision via numerical quadrature (i.e., Riemann summation) over the actual geometries. For the present rudimentary analysis, we further simplify the analysis by assuming that the crater fill is a circular cylinder of diameter D and height h . In order to capture conditions resembling mid-latitude craters on Mars (and cases 1–5, Table I), we further generalize the analysis by using the ratio $D/h = 30$ [8]. After substitution of the model (18), Eq. (21) becomes

$$\delta t = \frac{\rho_s g D^2}{3C\rho u_\tau^3(1/4 + \alpha D)}. \quad (22)$$

For the present purposes, we have further simplified Eq. (22) by removing the threshold control on saltation activity. Since we

are not trying to model actual landscape morphodynamics but rather perform an order-of-magnitude analysis, the threshold control can be removed without loss of generality. Equation (22) first shows that $\delta t \sim u_\tau^{-3}$, highlighting the dramatic enhancement of mass excavation with even moderate increases in prevailing meteorological forcing. The Eq. (22) scaling dependence on u_τ is valid, but it has been comprehensively shown that u_τ is constantly changing aloft the crater basin due to turbulent fluctuations. Indeed, recall the Sec. III G material and the global wavelet spectrum profiles in Fig. 16, which demonstrated that the spectral density of $\bar{u}'(x_2, t)$ was concentrated at a frequency that was controlled by vortex shedding from the rim. From this we conclude that elevated u_τ and associated aeolian erosion are not active at all times and instead occur periodically as large helical vortices advect through the basin. It is thus prudent to rescale the Eq. (22) time scale, taking into account the periodic passage of these vortices. We can readily account for the periodic advection of coherent rollers by introducing two frequencies: one for the frequency of vortex production f_1 and another for the turnover frequencies of these eddies themselves f_2 . Figure 16 has shown that f_1 can be derived via introduction of the high-Reynolds-number Strouhal number St : $f_1 = StU_0h^{-1}$. Here f_2 can be estimated based on the advective velocity U_0 and a characteristic scale for these eddies. Fortunately, the only sensible length scale for produced vortices is h , and $f_2 = U_0h^{-1}$. With this, we can compute an exposure factor $\gamma = f_2/f_1 = St^{-1}$, yielding a deflation time δt^* rescaled for the passage of rollers with frequency f_2 , passing through the domain at frequency f_1 :

$$\delta t^* = \gamma \delta t. \quad (23)$$

For the present purposes, $\gamma = St^{-1} = 4$. Figure 17 shows the time needed to empty a crater with $D/h = 30$ and $D = 150 \text{ km}$, for a range of shear velocities and densities, as outlined in the figure. We used $C = 1$, $\rho_s = 3000 \text{ kg m}^{-3}$, $g = 3.7 \text{ m s}^{-2}$, and $\alpha = 10^{-5} \text{ m}^{-1}$. For reference, we superimposed $\delta t = 3.5 \times 10^9 \text{ yr}$, corresponding to the approximate Noachian-Hesperian boundary. Since $\delta t^* \sim \rho^{-1}$ and $\delta t^* \sim u_\tau^{-3}$, increasing either parameter results in a quicker excavation. Since the actual values on Mars over the Noachian-Hesperian boundary time scale are unknown, we considered a plausible range for each. Nonetheless, the present arguments support the overarching hypothesis that aeolian processes have played a major role in erosion of these large mid-latitude craters.

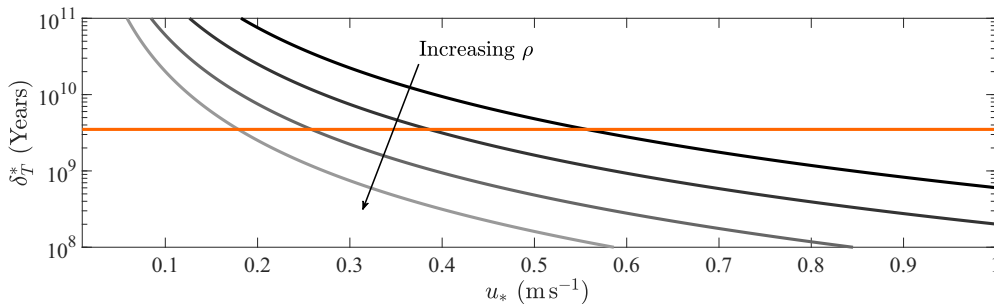


FIG. 17. Profiles of require time δ_T (years) to excavate the sedimentary fill of a once-filled crater under ambient planetary boundary layer forcing u_τ (m s^{-1}). Profiles correspond to varying atmospheric density: black, $\rho = 1 \times 10^{-3} \text{ kg m}^{-3}$; dark gray, $\rho = 3 \times 10^{-3} \text{ kg m}^{-3}$; light gray, $\rho = 1 \times 10^{-2} \text{ kg m}^{-3}$; and lightest gray, $\rho = 3 \times 10^{-2} \text{ kg m}^{-3}$. The horizontal orange line at $\delta_T = 3.5 \times 10^9 \text{ yr}$ denotes the approximate Noachian-Hesperian boundary.

IV. CONCLUSION

Central mounds composed of sedimentary strata are found within craters on Mars [4], which record geological history of processes on Mars. For mid-latitude craters, the central mound is thought to be the result of long-term aeolian weathering [8–10], a hypothesis thoroughly supported by systematic evaluation of aeolian wind markers in Gale Crater [11], the landing site of the Curiosity rover [1,2]. Intracrater circulations associated with vortex shedding from the crater upwind rim, followed by vortex realignment within the basin, have been attributed to establishing the geometric pattern of radial moat formation.

In this work, a series of detailed LES cases have been used to capture flow processes aloft synthetic craters at five deflationary stages, from a filled (early) crater, to an empty (late) crater. Rigorous post processing of the LES data sets confirmed the hypotheses put forward on the role of counterrotating helical vortices in aeolian erosion of the basin fill, while some additional analysis revealed the profound influence of turbulent fluctuations in emptying the crater.

Specifically, a review of constituent terms within the Reynolds-averaged vorticity transport equation revealed that the intracrater circulations receive sustenance from spatial heterogeneity of the Reynolds stresses; that is, the circulations are a turbulent secondary flow [40], with the stretching-and-tilting terms making a relatively lesser contribution to the vortices. This is important, since models for aeolian saltation and dust emissions exhibit dramatic scaling upon aerodynamic drag $Q \sim u_\tau^3$ and $F \sim u_\tau^4$ [12,44]. With this result, we generated PDFs from time-series velocity at discrete locations aloft the basin, all of which confirmed the wide variability (heavy tails) in velocity fluctuations, and these PDFs were used to guide selection of a low-frequency high-magnitude threshold for conditional sampling of the flow. The conditionally sampled flow fields revealed that during high-magnitude fluctuations, two intracrater helical vortices are present. We subsequently presented a structural model of flow aloft the basin, using the vorticity dynamics analysis to summarize the mechanisms responsible for sustenance of the streamwise vortices at different locations.

We also generated contours of the Reynolds- and conditionally averaged surface stress, which showed how the process of aeolian emptying was initiated via formation of two upwind recessions. The deflationary trajectory proceeds following formation of the two recessions, which connect to form a crescentic depression that slowly grows in the azimuthal direction while also deepening. This result, in particular,

is helpful to understand the complementary influence of katabatic winds and crater circulations in emptying the crater. While katabatic winds sustained by buoyancy gradients and landscape relief are prominent in aeolian morphodynamics once the moat has been formed, these winds could not have initiated the emptying process when the basin was filled. Results in this article show how the shedding of helical vortices initiated the process. Finally, we used the results of wavelet decomposition to rescale an estimated deflationary time scale for crater emptying. When representative parameters for atmospheric conditions and aeolian models were used, we were able to demonstrate that a model basin with geometric extent modeled after Gale Crater could have been emptied by aeolian processes.

We emphasize that insights gained from this work could only be derived from LES. For example, the generation of probability density functions (Sec. III C), from which the conditionally averaged flow fields were attained (Sec. III D), is contingent upon discrete time-varying flow statistics; such statistics are not resolved during Reynolds-averaged Navier Stokes simulation. Similarly, the joint time-frequency decomposition presented in Sec. III G required time-varying input arguments, and these results were used in the rudimentary assessment of crater excavation capacity in Sec. III H.

Under the action of radial katabatic winds, the crater basins serve as sites for the formation of cold pools, which grow in depth during the evening hours as cold heavy fluid is continuously transported in the direction of greatest relief. Cold pools can be disrupted by shear aloft the basin, where a Froude number $Fr = U/NL$, constructed from velocity and length scales U and L , respectively, and Brunt-Väisälä frequency N can be used to determine whether or not the cold pool will be homogenized [57–59]. Due to the lack of an available N for large, mid-latitude craters in Mars, it is difficult to speculate on how cold pools may inhibit aeolian morphodynamics within the crater. It has certainly been shown that these effects are important on a smaller terrestrial crater [22].

ACKNOWLEDGMENTS

W.A. was supported via start-up package provisions from the University of Texas at Dallas. Computational resources were provided by the Texas Advanced Computing Center at the University of Texas at Austin. The authors thank Gary Kocurek, UT Austin, for providing numerous helpful comments on this work.

-
- [1] J. Grotzinger *et al.*, *Science* **343**, 1242777 (2014).
 - [2] J. Grotzinger *et al.*, *Science* **350**, 7575 (2015).
 - [3] M. C. Palucis, W. E. Dietrich, R. M. E. Williams, A. G. Hayes, T. Parker, D. Y. Sumner, N. Mangold, K. Lewis, and H. Newsom, *J. Geophys. Res.* **121**, 472 (2016).
 - [4] K. Bennett and J. Bell, *Icarus* **264**, 331 (2016).
 - [5] M. Malin and K. Edgett, *Science* **290**, 1927 (2000).
 - [6] C. Fassett and J. Head, *Icarus* **198**, 37 (2008).

- [7] J. P. Grotzinger and R. E. Milliken, in *Sedimentary Geology of Mars*, edited by J. P. Grotzinger and R. E. Milliken, SEPM Special Publication Vol. 102 (SEPM Society for Sedimentary Geology, Tulsa, 2012), p. 1.
- [8] M. Day, W. Anderson, G. Kocurek, and D. Mohrig, *Geophys. Res. Lett.* **43**, 2473 (2016).
- [9] E. Kite, K. Lewis, M. Lamb, C. Newman, and M. Richardson, *Geology* **41**, 543 (2013).

- [10] E. Kite, J. Sneed, D. Mayer, K. Lewis, T. Michaels, A. Hore, and S. Rafkin, *J. Geophys. Res.* **121**, 2282 (2016).
- [11] M. Day and G. Kocurek, *Icarus* **280**, 37 (2016).
- [12] J. Kok, E. Parteli, T. Michaels, and D. Karam, *Rep. Prog. Phys.* **75**, 106901 (2012).
- [13] T. Pahzt, J. Kok, and H. Herrmann, *New J. Phys.* **14**, 043035 (2012).
- [14] R. Kuzmin, R. Greeley, S. Rafkin, and R. Haberle, *Icarus* **153**, 61 (2001).
- [15] A. Petrosyan, B. Galperin, S. Larsen, S. Lewis, A. Maattanen, P. Read, N. Renno, L. Rogberg, H. Savijarvi, T. Siili, A. Spiga, A. Toigo, and L. Vazquez, *Rev. Geophys.* **49**, RG3005 (2011).
- [16] L. Fenton, J. Bandfield, and A. Ward, *J. Geophys. Res.* **108**, 5129 (2003).
- [17] L. Fenton and R. Hayward, *Geomorphology* **121**, 98 (2010).
- [18] M. Almeida, E. Parteli, J. Andrade, and H. Herrmann, *Proc. Natl. Acad. Sci. USA* **105**, 6222 (2008).
- [19] J. Kok, *Phys. Rev. Lett.* **104**, 074502 (2010).
- [20] F. Ayoub, J.-P. Avouac, C. Newman, M. Richardson, A. Lucas, S. Leprince, and N. Bridges, *Nat. Commun.* **5**, 5096 (2014).
- [21] M. Chan and D. Netoff, *Geophys. Res. Lett.* **44**, 4000 (2017).
- [22] C. Whiteman, S. Hoch, M. Hahnenberger, A. Muschinski, V. Hohreiter, M. Behn, Y. Cheon, S. Zhong, W. Yao, D. Fritts, C. Clements, T. Horst, W. Brown, and S. Oncley, *Bull. Am. Meteor. Soc.* **89**, 1665 (2008).
- [23] M. Katurji, S. Zhong, M. Kiefer, and P. Zavar-Reza, *J. Geophys. Res.* **118**, 6052 (2013).
- [24] J. Albertson and M. Parlange, *Water Resour. Res.* **35**, 2121 (1999).
- [25] W. Anderson and C. Meneveau, *Bound.-Layer Meteorol.* **137**, 397 (2010).
- [26] E. Bou-Zeid, C. Meneveau, and M. Parlange, *Phys. Fluids* **17**, 025105 (2005).
- [27] S. Chester, C. Meneveau, and M. Parlange, *J. Comput. Phys.* **225**, 427 (2007).
- [28] J. Smagorinsky, *Mon. Weather Rev.* **91**, 99 (1963).
- [29] C. Meneveau and J. Katz, *Annu. Rev. Fluid Mech.* **32**, 1 (2000).
- [30] S. Orszag, *J. Atmos. Sci.* **27**, 890 (1970).
- [31] W. Anderson, *Int. J. Numer. Methods Fluids* **71**, 1588 (2012).
- [32] J. Deardorff, *J. Fluid Mech.* **41**, 453 (1970).
- [33] U. Piomelli and E. Balaras, *Annu. Rev. Fluid Mech.* **34**, 349 (2002).
- [34] W. Brutsaert, *Hydrology: An Introduction* (Cambridge University Press, Cambridge, 2005).
- [35] E. Bou-Zeid, M. Parlange, and C. Meneveau, *J. Atmos. Sci.* **64**, 216 (2007).
- [36] Q. Li, E. Bou-Zeid, and W. Anderson, *J. Comput. Phys.* **310**, 237 (2016).
- [37] R. Antonia, *Annu. Rev. Fluid Mech.* **13**, 131 (1981).
- [38] C. Jacob and W. Anderson, *Boundary-Layer Meteorol.* **162**, 22 (2017).
- [39] F. M. White, *Fluid Mechanics* (McGraw-Hill, New York, 1999).
- [40] P. Bradshaw, *Annu. Rev. Fluid Mech.* **19**, 53 (1987).
- [41] J. Mansfield, O. Knio, and C. Meneveau, *J. Comput. Phys.* **145**, 693 (1998).
- [42] J. Mansfield, O. Knio, and C. Meneveau, *J. Comput. Phys.* **152**, 305 (1999).
- [43] R. Bagnold, *The Physics of Blown Sand and Desert Dunes* (Chapman and Hall, London, 1956).
- [44] Y. Shao, *Physics and Modelling of Wind Erosion* (Springer, Berlin, 2008).
- [45] J. Kim, P. Moin, and R. Moser, *J. Fluid Mech.* **177**, 133 (1987).
- [46] R. Adrian, *Zoran P. Zaric Memorial International Seminar on Near-Wall Turbulence* (Hemisphere, Washington, DC, 1988).
- [47] J. Sheng, E. Malkiel, and J. Katz, *J. Fluid Mech.* **633**, 17 (2009).
- [48] J. Finnigan, R. Shaw, and E. Patton, *J. Fluid Mech.* **637**, 387 (2009).
- [49] N. Hutchins, J. P. Monty, B. Ganapathisubramani, H. C. H. Ng, and I. Marusic, *J. Fluid Mech.* **673**, 255 (2011).
- [50] D. Richter and P. Sullivan, *Phys. Fluids* **26**, 103304 (2014).
- [51] S. Pope, *Turbulent Flows* (Cambridge University Press, Cambridge, 2000).
- [52] L. Cohen, *Proc. IEEE* **77**, 941 (1989).
- [53] M. Farge, *Annu. Rev. Fluid Mech.* **24**, 395 (1992).
- [54] P. Owen, *J. Fluid Mech.* **20**, 225 (1964).
- [55] D. Gillette and R. Passi, *J. Geophys. Res.* **93**, 14233 (1988).
- [56] B. Marticorena and G. Bergametti, *J. Geophys. Res.* **100**, 16415 (1995).
- [57] R. Bell and R. Thompson, *J. Fluid Mech.* **96**, 757 (1980).
- [58] K. Kitabayashi, *J. Meteorol. Soc.* **55**, 193 (1977).
- [59] G. Poulos, J. Bossert, T. McKee, and R. Pielke, *J. Atmos. Sci.* **57**, 1919 (2000).